

Review

Open Access



# Recent advances in 2D structured materials with defect-exploiting design strategies for electrocatalysis of nitrate to ammonia

Jinuk Choi<sup>1,†</sup>, Sejin Im<sup>1,†</sup>, Jihyun Choi<sup>1</sup>, Subramani Surendran<sup>1</sup>, Dae Jun Moon<sup>1,2</sup>, Joon Young Kim<sup>1,2</sup>, Jung Kyu Kim<sup>3,4</sup>, Uk Sim<sup>1,2,4,†</sup>

<sup>1</sup>Hydrogen Energy Technology Laboratory, Korea Institute of Energy Technology (KENTECH), Jeonnam 58330, Republic of Korea.

<sup>2</sup>Research Institute, NEEL Sciences, INC., Jeollanamdo 58326, Republic of Korea.

<sup>3</sup>School of Chemical Engineering, Sungkyunkwan University (SKKU), Suwon 16419, Republic of Korea.

<sup>4</sup>Center for Energy Storage System, Chonnam National University, Gwangju 61186, Republic of Korea.

<sup>†</sup>Authors contributed equally.

**\*Correspondence to:** Prof. Jung Kyu Kim, School of Chemical Engineering, Sungkyunkwan University (SKKU), 2066 Seobu-ro, Jangan-gu, Suwon 16419, Republic of Korea. E-mail: legkim@skku.edu; Prof. Uk Sim, Hydrogen Energy Technology Laboratory, Korea Institute of Energy Technology (KENTECH), 200 Hyeoksin-ro, Naju, Jeonnam 58330, Republic of Korea. E-mail: usim@kentech.ac.kr

**How to cite this article:** Choi J, Im S, Choi J, Surendran S, Moon DJ, Kim JY, Kim JK, Sim U. Recent advances in 2D structured materials with defect-exploiting design strategies for electrocatalysis of nitrate to ammonia. *Energy Mater* 2024;4:400020. <https://dx.doi.org/10.20517/energymater.2023.67>

**Received:** 31 Aug 2023 **First Decision:** 8 Oct 2023 **Revised:** 24 Nov 2023 **Accepted:** 15 Jan 2024 **Published:** 15 Mar 2024

**Academic Editor:** Hao Liu **Copy Editor:** Fangyuan Liu **Production Editor:** Fangyuan Liu

## Abstract

Ammonia has been used in a wide variety of applications, and with the recent interest in hydrogen energy as a green energy source, it is emerging as a cost-effective, high-density hydrogen carrier due to its three hydrogen atoms. Currently, ammonia is produced by the Haber-Bosch method at high temperatures and pressure, which is energy-intensive and emits large amounts of carbon dioxide. As a viable alternative, the electrochemical conversion of nitrate to ammonia has emerged as an efficient and eco-friendly synthesis method. To encourage further exploration in this field, this review offers insights into utilizing two-dimensional materials as electrochemical catalysts, focusing on designs that exploit defects for nitrate reduction to ammonia.

**Keywords:** Nitrate reduction reaction, ammonia synthesis, 2D electrocatalyst, defect engineering

## INTRODUCTION

As the world transitions to a renewable energy and hydrogen (H<sub>2</sub>) economy to achieve a carbon-neutral



© The Author(s) 2024. **Open Access** This article is licensed under a Creative Commons Attribution 4.0 International License (<https://creativecommons.org/licenses/by/4.0/>), which permits unrestricted use, sharing, adaptation, distribution and reproduction in any medium or format, for any purpose, even commercially, as long as you give appropriate credit to the original author(s) and the source, provide a link to the Creative Commons license, and indicate if changes were made.



society, ammonia is gaining traction as a hydrogen carrier<sup>[1,2]</sup> and carbon-free fuel<sup>[3,4]</sup> for hard-to-decarbonize sectors such as power generation<sup>[5,6]</sup> and transportation<sup>[7,8]</sup>. Unlike hydrogen, which liquefies at around -253 °C, ammonia liquefies at -34 °C, making it easy to store and transport [Table 1]<sup>[9,10]</sup>. Globally, about 180 million tons of ammonia are produced yearly<sup>[11]</sup>, of which 80% is used as a fertilizer for agriculture, and the remaining 20% is used in explosives, pharmaceuticals, and more<sup>[12]</sup>. Ammonia is produced under high temperature and pressure conditions (350-550 °C, 150-250 bar) via the Haber-Bosch process, which is an energy-intensive procedure that requires 1%-2% of the total energy produced by humans on the earth<sup>[13]</sup> [Figure 1A]. In addition, the amount of methane consumed in the production process is about 3.5 times higher, and more than 400 million tons of CO<sub>2</sub> is emitted annually to produce ammonia, which can cause environmental problems<sup>[14]</sup>.

Electrochemical ammonia production has been proposed as an alternative to the Haber-Bosch process and is gaining traction due to several advantages [Figure 1B]. First, it is energy efficient, as ammonia can be produced under ambient conditions, as opposed to the high temperature and pressure conditions of the Haber-Bosch method<sup>[15]</sup>; Second, it is environmentally friendly as it can be combined with renewable energy sources (solar, tidal, and wind) with low carbon emissions<sup>[16]</sup>; Third, it uses nitrogen and water as reactants, eliminating the use of fossil fuels as a source of H<sub>2</sub>, with the required protons (H<sup>+</sup>) generated on-site through the oxidation of water<sup>[17]</sup>. Finally, the process has advantages such as flexible reaction control<sup>[18]</sup>, scalability, and on-demand on-site NH<sub>3</sub> production<sup>[19]</sup>. Electrochemical ammonia synthesis is mainly based on nitrogen reduction reactions (NRR)<sup>[20,21]</sup>, and although many preliminary results have been obtained, the low efficiency has limited its commercialization<sup>[22]</sup>. To overcome this limitation, electrochemical ammonia synthesis using the ionic states of nitrogen oxides has recently been investigated<sup>[23-27]</sup>.

From the nitrogen cycle, nitrogen oxides are stable forms under normal aerobic conditions<sup>[28]</sup>; however, as the accumulation of nitrogen oxides increases due to industrial activities, it causes health problems such as liver damage<sup>[29]</sup> and blue baby<sup>[30]</sup>. To restore the nitrogen cycle, the World Health Organization (WHO) stated that the maximum tolerable concentration of NO<sub>3</sub><sup>-</sup> in water and wastewater is 50 mg/L<sup>[31]</sup>. For the removal of nitrogen oxides, physical removal methods are still used, such as reverse osmosis<sup>[32]</sup> or ion exchange<sup>[33]</sup>; however, these costs are high, about \$1-2 million per year per city (based on a population of 500,000 in the US)<sup>[34]</sup>.

Recently, nitrate reduction reaction (NitRR), also known as NO<sub>3</sub>RR, has been studied due to its ability to synthesize ammonia and remove pollutants simultaneously<sup>[35,36]</sup>. In addition, following advantages over nitrogen, the solubility of NO<sub>2</sub><sup>-</sup> or NO<sub>3</sub><sup>-</sup> is about 40,000 times that of N<sub>2</sub> gas, and the dissociation of N-O (204 kJ/mol) compared to N≡N (945 kJ/mol) is much easier, making NitRR more economical than NRR<sup>[37,38]</sup>. As a result, the total conversion and energy efficiency of NitRR is much higher than NRR, and its performance can be further improved by strategic catalyst design. NitRR mechanisms involve nine protons, eight electrons, and reaction pathways depending on the reaction conditions<sup>[39]</sup>. Due to their complex pathways, NitRR to ammonia has a variety of by-products, such as N<sub>2</sub>, NO, and NO<sub>2</sub><sup>-</sup>, which increases the difficulty of analyzing the mechanism<sup>[40]</sup>. Various papers have revealed the mechanism, selectivity, and activity of NitRR. In previous studies, the rate-determining step (RDS) of NitRR is generally known to be NO<sub>3</sub><sup>-</sup> to NO<sub>2</sub><sup>-</sup> on transition metal (TM) surfaces and under acidic conditions<sup>[41]</sup>. The RDS can be seen in Figure 2. To increase the efficiency of the overall NitRR, it is necessary to develop a catalyst that facilitates the adsorption/desorption of NO<sub>3</sub><sup>-</sup>. The metal-based catalysts, such as Pt<sup>[42]</sup>, Pd<sup>[43]</sup>, Ag<sup>[44]</sup>, Sn<sup>[45]</sup>, and Cu-based catalysts<sup>[46-48]</sup>, are considered universal selections in the electrocatalytic process to lower the NitRR overpotential due to their high activity and appropriate adsorption energy of nitrate<sup>[49]</sup>. These are verified theoretically by the online differential electrochemical mass spectrometry (DEMS) and density functional theory (DFT) calculation<sup>[43,46,48]</sup>.

**Table 1. Comparison of liquid hydrogen and liquid ammonia**

Properties	Unit	Liquid hydrogen	Liquid ammonia	Ref.
Density	kg/m <sup>3</sup>	70.6	682	[13]
Transported temperature, pressure	°C, bar	-253, 1.2 bar	-33, 1 bar	[13]
The gravimetric energy density (LHV)	MJ/kg	120	18.6	[14]
Volumetric energy density (LHV)	MJ/L	8.49	12.7	[14]
Gravimetric hydrogen content	wt%	100	17.8	[14]
Volumetric hydrogen content	kg H <sub>2</sub> /m <sup>3</sup>	70.8	121	[14]
Explosive limit in air	vol%	18.3-59	16-25	-
Storage method		Liquefaction	Liquefaction	-

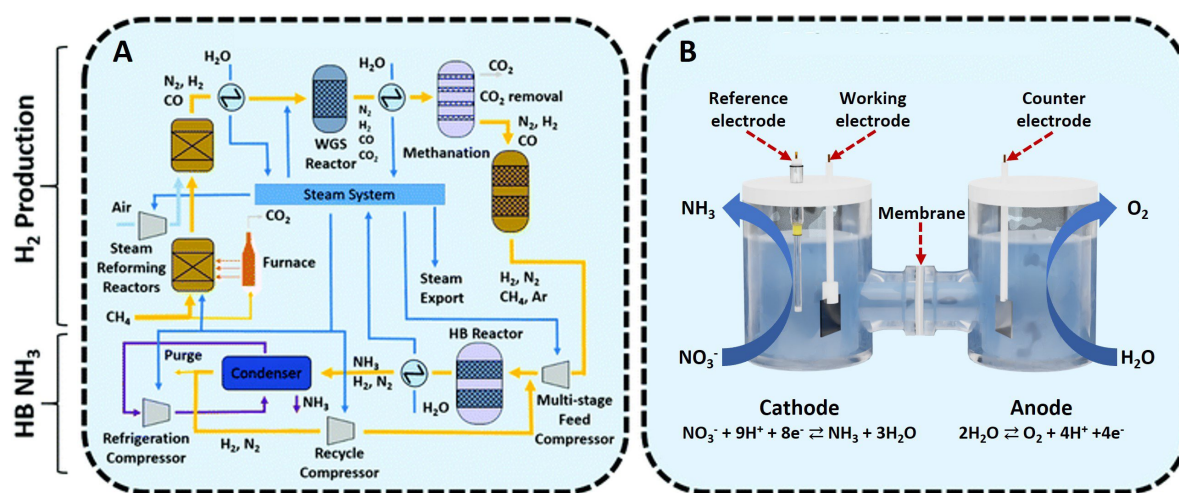


**Figure 1.** Schematic diagrams of ammonia synthesis. (A) The Haber-Bosch process (Reprinted with permission from Ref. [27]. Copyright 2019 Royal Society of Chemistry) [27] and (B) The electrochemical synthesis of ammonia process.

Over the past decade, there has been increasing interest in atomistic, low-cost two-dimensional (2D) nanosheet materials with unique physicochemical properties, such as high specific surface area, desirable morphology with myriad binding sites, and excellent reaction rates due to fast ion diffusion pathways [50]. In particular, 2D nanosheets are promising materials for catalysis due to their high surface efficiency [51], which can be exposed to active sites. Many studies have been conducted on layered double hydroxides (LDH) [52,53], chalcogenides [54,55], MXenes [56,57], metal-organic frameworks (MOFs) [58,59], *etc.* [60-62]. These 2D materials have found applications as catalysts or substrates, leveraging their intrinsic properties such as conductivity and activity for NitRR. Certain 2D materials, such as graphene, show limited electrocatalytic properties for NitRR; however, they have high conductivity, rendering them more suitable as substrates than active materials. This enhances conductivity and creates a synergy effect when used with functional materials.

To synthesize efficient electrocatalysts, porosity engineering is critical in carrying abundant active sites and shortened channels through meso-/macropores for mass/charge transport [63]. Also, the oxygen vacancy (OV) [64,65] in oxides is used as a powerful strategy to regulate the crystalline structure, electronic structure, and surface properties. In addition, doping heteroatoms efficiently modifies the electron structure of electrocatalysts to decrease the value of  $\text{GH}^*\Delta$  of the electrocatalysts and to improve electrochemical activity [66]. It can make synergistic effects to boost mass transfer on 2D nanosheets and increase active sites through the multiscale defect. Moreover, the adjustment of interlayer spacing can not only tune the atomic

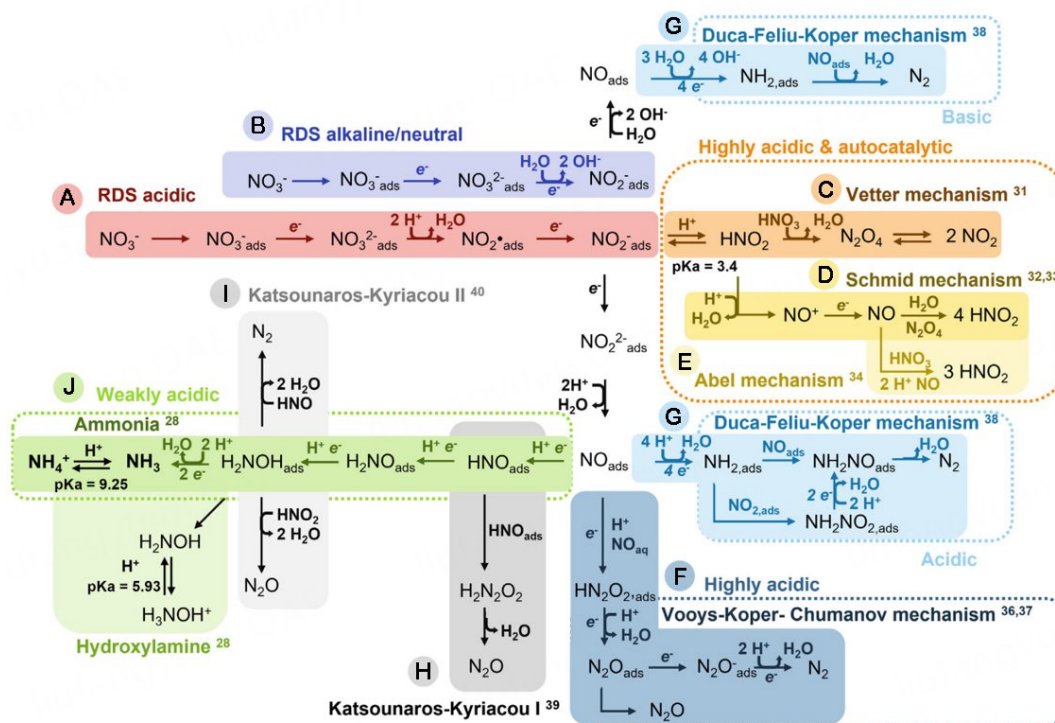


**Figure 2.** Schematic illustrations of the NitRR mechanisms (Reprinted with permission from Ref.<sup>[49]</sup>. Copyright 2022 Wiley-VCH GmbH)<sup>[49]</sup>.

distance and electron interaction but also manipulate the electronic structure of host materials, promising higher electrical conductivity<sup>[54]</sup>. Therefore, design strategies for electrocatalysts make it very possible to modulate the binding strength of intermediates, such as  $\text{NO}_2^-$ , and the competitive hydrogen evolution reaction (HER) process in NitRR.

In this review, we provide an overview of 2D materials as electrochemical catalysts and report the latest results of applying defects, such as doping, OVs, and topological defects, to enhance their activity as electrocatalysts in the electrochemical synthesis of ammonia. We also present our views on future research directions for ultrathin 2D materials to encourage further active research.

## 2D STRUCTURE ELECTROCATALYSTS: DEFECT ENGINEERING

### Layered double hydroxides

The earth-abundant TM catalysts have been focused on overcoming the disadvantages of noble metal catalysts. However, the TMs quickly form M-H bonds, leading to low Faradaic efficiency (FE) and poor selectivity of  $\text{NH}_3$ <sup>[67,68]</sup>. High HER performance makes NitRR performance soft because HER is a competitive reaction with NitRR. Moreover, another problem exists in that  $\text{NO}_3^-$  has an innately lower binding affinity with TMs in the aqueous solution because of strong hydrogen bonding and its symmetrical resonant structure<sup>[47]</sup>. Recently, TM-based LDHs (TM LDHs,  $[\text{M}_{1-x}\text{M}'_x(\text{OH})_2]^{x+}(\text{A}^{n-})_{x/n} \cdot m\text{H}_2\text{O}$ ), sometimes called Hydrotalcite-like compounds (HTLCs), have been focused on NitRR fields. The TM LDH consists of divalent ( $\text{M}^{2+}$ : e.g.,  $\text{Ni}^{2+}$ ,  $\text{Mg}^{2+}$ , or  $\text{Zn}^{2+}$ ) and trivalent ( $\text{M}'^{3+}$ , e.g.,  $\text{Mn}^{3+}$ ,  $\text{Fe}^{3+}$ , and  $\text{Al}^{3+}$ ) metal cations with interlayer exchangeable inorganic or organic anions ( $\text{A}^{n-}$ : e.g.,  $\text{NO}_3^-$ ,  $\text{SO}_4^{2-}$ ,  $\text{CO}_3^{2-}$ , and  $\text{Cl}^-$ )<sup>[69]</sup>. TM LDH catalysts have many advantages, such as large surface area, active site, low cost, easily tunable electric structure, and chemical composition<sup>[70]</sup>. The various synthesis methods of TM LDHs have been researched

because of their unique 2D structure. The exfoliation method belongs to the top-down method and is usually used to make 2D materials, including TM LDH nanosheets. Other top-down synthesis methods have been studied, such as plasma etching and liquid exfoliation. Otherwise, bottom-up methods also have attention owing to their relatively simple process. Microemulsion, Coprecipitation, and hydrothermal processes were representative bottom-up methods to synthesize TM LDH nanosheets<sup>[71-73]</sup>. TM LDH catalysts could be easily synthesized through a one-step or two-step hydrothermal process<sup>[70]</sup>.

TM LDH catalysts can easily apply reforming methods to improve performance due to their intrinsic 2D structure. Distortion is a frequently used method in 2D materials, leading to a distorted surface, which can cause more exposure of the edge site to enhance electrocatalytic performance. OVs are one of the representative defect engineering methods used to improve the electrochemical properties in the TM LDH catalysts by boosting the charge transfer/separation and optimizing the reaction kinetics. These vacancies also make TM LDH catalysts higher electrical conductivity and increase adsorption for oxygen-based intermediates<sup>[74]</sup>. Recently, the hybrid TM LDH-based catalysts for NitRR, including two kinds of metal, have been studied in most research. These mixed TM LDH catalysts show good reactive performance due to synergistic effects. Du *et al.* efficiently synthesized the CoFe LDH catalysts with the hydrothermal method in **Figure 3A**, and the catalyst performed excellent FE, NH<sub>3</sub> selectivity, high activity, and durability in alkaline conditions<sup>[52]</sup>. The DFT calculations indicated that CoFe LDH has a downhill reaction step (NO<sub>3</sub><sup>-</sup> → \*NO<sub>3</sub><sup>-</sup> → \*NO<sub>2</sub><sup>-</sup>) free energy and a moderate desorption step (\*NH<sub>3</sub> → NH<sub>3</sub>) free energy compared to that of Co LDH and Fe LDH [**Figure 3B**]. NH<sub>3</sub> selectivity and FE of CoFe LDH shows 98.93% and 97.68% at -0.45 V (vs. reversible hydrogen electrode (RHE)) in 1 M KOH and 1,400 ppm NO<sub>3</sub><sup>-</sup> electrolytes [**Figure 3C**]. The operation durability of performance of the CoFe LDH in NitRR maintained for 12 cycles with 36 h in **Figure 3D**. To increase the conductivity of TM LDH catalysts, TM LDH-decorated Cu foam electrodes have been studied by Kim *et al.*<sup>[53]</sup>. The Ni<sub>3</sub>Fe-CO<sub>3</sub> LDH/Cu achieved the NH<sub>3</sub> selectivity of 95.8%, the NH<sub>3</sub> productivity of 1.261 mg h<sup>-1</sup> cm<sup>-2</sup>, and FE of 96.8% at -0.2 V (vs. RHE) in 1 M KOH electrolytes with 5 mM KNO<sub>3</sub> [**Figure 3E and F**]. Various multi-TM LDH/Cu foams were used as electrocatalysts to compare the electrocatalyst performance. Among them, Ni<sub>3</sub>Fe-CO<sub>3</sub> LDH/Cu foam shows the highest electrocatalytic performance [**Figure 3G**]. The catalyst suppresses H-H bond formation by hindering the Heyrovsky step (H<sub>ads</sub><sup>\*</sup> + H<sub>2</sub>O + e<sup>-</sup> → H<sub>2</sub> + OH<sup>-</sup>) relating to the Volmer step (H<sub>2</sub>O + e<sup>-</sup> → H<sub>ads</sub><sup>\*</sup> + OH<sup>-</sup>). Ternary TM LDH catalysts have been studied to apply complementary effects. Li *et al.* investigated Cu<sub>2</sub>CoAl LDH catalyst for NitRR [**Figure 3H**]<sup>[75]</sup>. The Cu/Al LDHs show lower structural stability than Co/Al LDH because of the Jahn-Teller effect. However, the Cu-based catalyst has a higher electrocatalytic activity for NitRR than the Co-based catalyst. Cu<sub>2</sub>CoAl LDH was synthesized to utilize each advantage, and the catalyst shows an NH<sub>3</sub> conversion of 83% at -0.74 V (vs. Hg/HgO) in 1 M NaOH electrolytes with 0.1 M NaNO<sub>3</sub> in **Figure 3I**. Therefore, research into TM LDHs as electrocatalysts has significantly advanced owing to their large active area and cost-effective manufacturing. They can be applied concurrently with defect engineering during hydrothermal processes. Thus, due to their low manufacturing cost, a simple synthesis system holds high potential for commercializing the TM LDH catalyst in the industry.

### Chalcogenides

The low-cost TM chalcogenide materials have been considered to replace the high-cost precious metal catalysts. A TM chalcogenide is a chemical compound of at least one TM cation and at least one more chalcogen anion (S, Se, and Te). Among the TM chalcogenides, TM dichalcogenides (TMDs), such as metal disulfides (MS<sub>2</sub>) and diselenides (MSe<sub>2</sub>), with M<sup>4+</sup> (Mo<sup>4+</sup>, Ti<sup>4+</sup>, and V<sup>4+</sup>) have been widely used in various electrochemical applications due to the unique physicochemical and structural features<sup>[76]</sup>. TMDs have unique layered structures, and one of them, TiS<sub>2</sub>, was investigated as a cathode material for secondary batteries because of its layered structure that can be intercalated by lithium in the 1970s<sup>[77]</sup>. In addition to these structure features, TMDs can be easily doped with various TMs to tune the electric structure and chemical composition<sup>[78]</sup>.

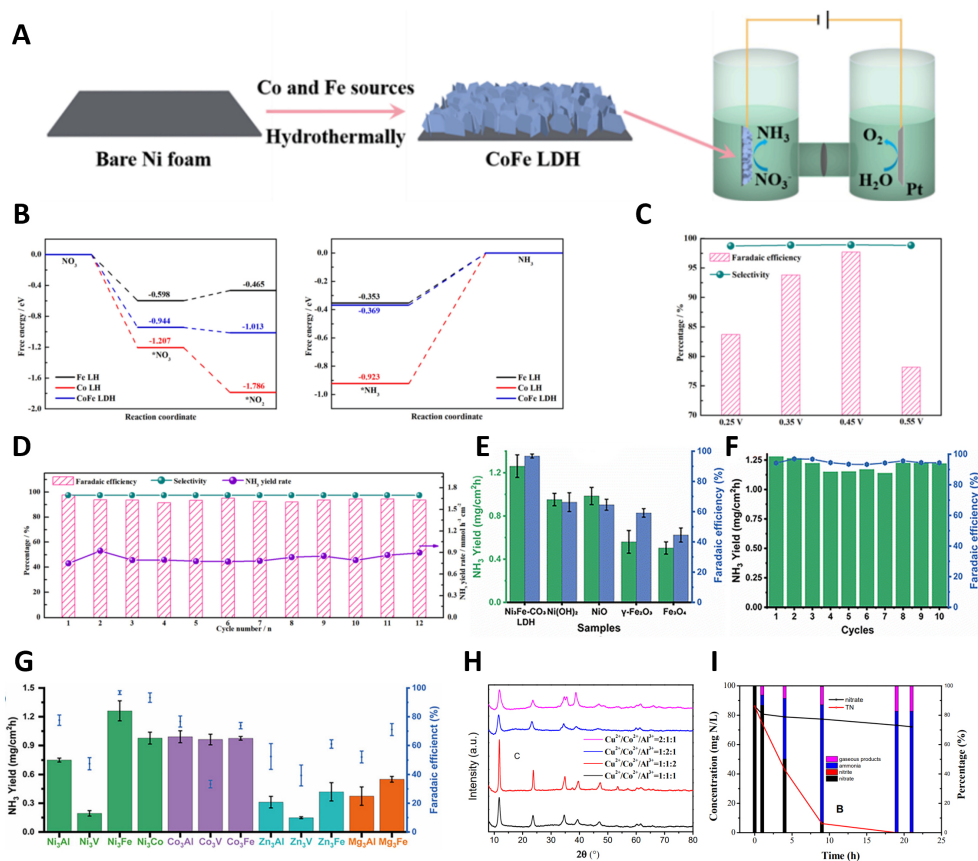


**Figure 3.** (A) Schematic image of the synthesis process for CoFe LDH and its cell composition for NitRR. (B) Reaction-free energies for  $^*NO_3$ ,  $^*NO_2$ , and  $^*NH_3$  on the Fe LH, Co LH, and CoFe LDH surfaces. (C) FE and  $NH_3$  selectivity of CoFe LDH according to potential. (D) The consecutive recycling test of CoFe LDH at  $-0.45$  V (vs. RHE). (A–D) Figures are reprinted with permission from Ref. [52]. Copyright 2022 Elsevier [52]. (E) Comparison of  $NH_3$  yield rate and FE of  $Ni_3Fe-Co_3$  LDH with reference materials. (F) The recycling test of  $Ni_3Fe-Co_3$  LDH/Cu foam electrode at  $-0.2$  V (vs. RHE). (G)  $NH_3$  yield rate and FE using multi-metallic TM LDH/Cu foam electrodes. (E–G) figures are reprinted with permission from Ref. [53]. Copyright 2023 The Royal Society of Chemistry [53]. (H) XRD patterns of Cu/Co/Al-HTLCs. (I) The transformation of  $NO_3^-$  and total nitrogen (TN) on Cu/Co/Al-HTLCs according to time at  $-0.74$  V (vs. RHE). (H and I) Figures are reprinted with permission from Ref. [75]. Copyright 2020 MDPI [75].

More recently, to improve the electrocatalytic performance, various nanostructures of TMDs have been studied. Partially, 2D TMDs exhibit the potential for NitRR owing to their large active area and tunable electronic structure. These 2D TMDs can be categorized into trigonal prismatic (hexagonal, H), octahedral (tetragonal, T), and distorted phase ( $T'$ ) [79]. Various defect engineering is also studied, and sulfur vacancies (SVs) are one of the representatives in the field of TMD catalysts [80].

Doping single metal atoms into 2D materials is considered one of the effective strategies to enhance the electrochemical performance of a catalyst [81,82]. Such strategies can significantly improve the electrochemical NitRR performance of a catalyst by incorporating metal dopants into 2D materials. Li *et al.* investigated the iron single atomic catalyst (SAC) supported on 2D  $MoS_2$  (Fe- $MoS_2$ ) nanosheets for NitRR [Figure 4A] [54]. Additionally, Cu-, Ni-, and Co- $MoS_2$  nanosheets were also studied to compare with Fe- $MoS_2$  catalysts, and Fe- $MoS_2$  has higher electrochemical performance than that of other catalysts [Figure 4B and C]. DFT studies show that Fe- $MoS_2$  presents the deoxidation of the  $^*NO$  to  $^*N$  intermediate, decreasing the energy barrier of the reaction pathway to synthesize ammonia. Ding *et al.* also studied Fe- $MoS_2$  catalysts through

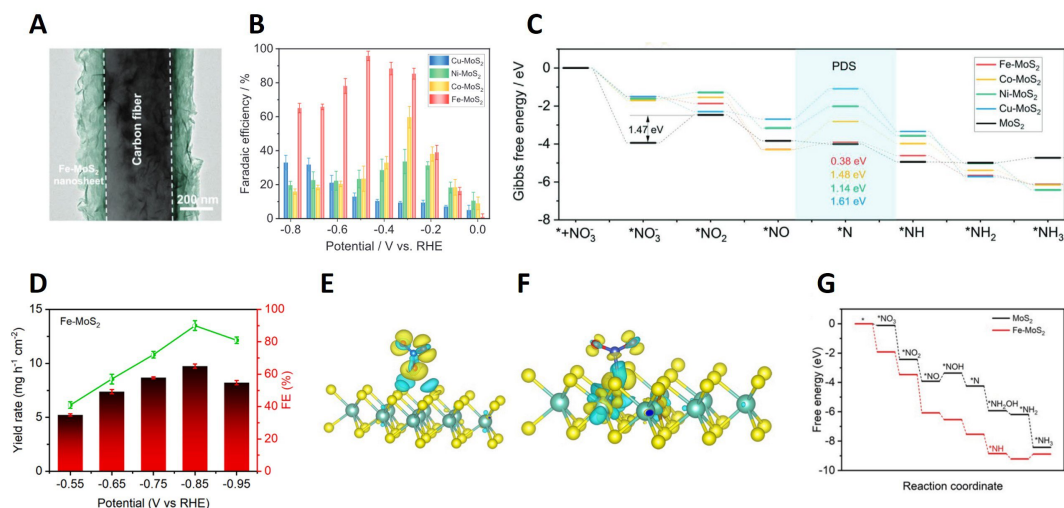


**Figure 4.** (A) TEM image of Fe-MoS<sub>2</sub> nanosheets on the carbon support. (B) FEs for NH<sub>3</sub> on Cu-MoS<sub>2</sub>, Ni-MoS<sub>2</sub>, Co-MoS<sub>2</sub>, and Fe-MoS<sub>2</sub> nanosheets at different potentials. (C) Reaction Gibbs free energies of intermediates on M-MoS<sub>2</sub> nanosheets. (A-C) figures are reprinted with permission from Ref.<sup>[54]</sup>. Copyright 2021 Wiley-VCH GmbH<sup>[54]</sup>. (D) Potential dependent NH<sub>3</sub> yield rate and FE of Fe-MoS<sub>2</sub>. Charge density difference results of NO<sub>3</sub><sup>-</sup> on (E) MoS<sub>2</sub> and (F) Fe-MoS<sub>2</sub>. (G) Reaction Gibbs free energies for NitRR on Fe-MoS<sub>2</sub> and MoS<sub>2</sub>. (D-G) Figures are reprinted with permission from Ref.<sup>[83]</sup>. Copyright 2023 Elsevier<sup>[83]</sup>.

DFT calculations for NitRR<sup>[83]</sup>. Since Fe on the MoS<sub>2</sub> improves the activating NitRR and suppressing HER, Fe-MoS<sub>2</sub> achieved a high FE of 90% and a yield rate of 9.75 mg h<sup>-1</sup> cm<sup>-2</sup> for NH<sub>3</sub> production at -0.85 V (vs. RHE) [Figure 4D]. Figure 4E and F show the charge density difference results, where the surface of Fe-MoS<sub>2</sub> has a lower NO<sub>3</sub><sup>-</sup> adsorption energy (-1.92 eV) than that of the surface of MoS<sub>2</sub> (-0.11 eV). The DFT results were calculated on the different pathways of NitRR, unlike the study above by Li *et al.*, Still, the Fe-MoS<sub>2</sub> reduces the energy barrier of the path, which is the protonation of \*NO to \*NOH intermediates in Figure 4G<sup>[54]</sup>. The 2D Cu-SnS<sub>2-x</sub> nanosheet arrays were investigated for NitRR by Li *et al.*<sup>[55]</sup>. Cu doping makes the abundant SVs on the SnS<sub>2</sub> nanosheet, which increases the electrocatalytic activity of the catalyst. The 2D Cu-SnS<sub>2-x</sub> nanosheet arrays showed two times higher NitRR performance, which is a yield rate of 0.63 mmol h<sup>-1</sup> mg<sub>cat.</sub><sup>-1</sup> and FE of 93.8% at -0.7 V (vs. RHE), than those of pristine SnS<sub>2</sub> in 0.1 M KOH with 0.1 M KNO<sub>3</sub> solution. The adsorption energy of Cu-SnS<sub>2-x</sub> (-1.6158 eV) is higher than that of SnS<sub>2-x</sub> (-2.0755 eV); however, the too-high adsorption energy may bring about difficulty in the desorption of the intermediaries according to Sabatier principle. DFT studies indicate that doped Cu stabilizes intermediates on the NitRR pathway and tunes the electron distribution. In addition, SVs enhance the adsorption capacity due to charge transfer to Sn. Thus, the TMDs have shown substantial promise for NitRR due to their advantages, including a large active area and tunable electronic structure. However, research in the NitRR field has primarily focused on a few TMD catalysts, such as MoS<sub>2</sub>, MoSe<sub>2</sub>, SnS<sub>2</sub>, and SeSe<sub>2</sub>, leaving various combinations of TMDs, including TaS<sub>2</sub>, NbS<sub>2</sub>, VS<sub>2</sub>, and MoTe<sub>2</sub>, largely unexplored. These catalysts offer unlimited potential for NitRR. Exploring other related materials is warranted to gain a more comprehensive understanding of 2D TMDs.

### Transition metal oxides

In the electrocatalytic field, low-cost TM oxide (TMO) catalysts have attracted attention for commercialization by replacing precious metal catalysts. TMO catalysts have many advantages, such as ease of synthesis, thermal and chemical stability, low cost, and high earth abundance to be used as catalysts<sup>[84]</sup>. However, these catalysts cannot be directly used for NitRR because TMOs have some disadvantages when used as catalysts because of their low electronic conductivity, relatively low active site, and low selectivity<sup>[85]</sup>.

Optimization strategies, such as nanostructure and defect engineering, have been considered to overcome these challenges and improve electrocatalytic performance. Nanostructure engineering is a process method for making catalysts have nanoscale structures, including nanoparticles and 2D structures. These structures increase the higher active area, narrow the band gap, and promote electronic conductivity<sup>[86]</sup>. Synthesizing 2D TMOs through the top-down method has challenges, leading to multiple attempts to explore the bottom-up method. For instance, Sun *et al.* and Sun *et al.* synthesize ultrafine 2D nanosheets of TMOs<sup>[87,88]</sup>. Huang *et al.* demonstrated the fabrication of graphene-like TMO nanosheets by utilizing graphene oxide (GO) as a 2D template, wherein metal precursors were deposited on the GO surface and then calcined<sup>[89]</sup>. Various TMs could synthesize 2D TMOs using either a 2D template or surfactant molecules. Defect engineering, such as OVs, is commonly used to improve NitRR performance with changes in electronic structure and surface properties. Standard modification methods, such as hydrogen heat treatment, thermal annealing, wet chemical reduction, and electroreduction, can quickly generate OVs in TMOs<sup>[65]</sup>.

Wang *et al.* studied Cu/CuO<sub>x</sub> in-plane heterostructured nanosheet arrays with OVs (Cu/CuO<sub>x</sub>/CF) for NitRR [Figure 5A]<sup>[60]</sup>. This 2D nanosheet structure has rich exposing active sites and high mass/charge transfer. Moreover, OVs and in-plane heterojunctions tune electronic structures and improve adsorption capabilities and properties. The test results show that Cu/CuO<sub>x</sub>/CF achieves higher electrocatalytic performance, FE of 93.58%, and an NH<sub>3</sub> production of 0.23 mmol h<sup>-1</sup> cm<sup>-2</sup> at -1.3 V (*vs.* saturated calomel electrode, SCE) than that of CuO<sub>x</sub>/CF, Cu/CF, and Cu Foam [Figure 5B and C]. For five cycles, the retention of the yield rate and FE of Cu/CuO<sub>x</sub>/CF was maintained at a high level in Figure 5D. Zhao *et al.* studied the modulation of multi-scale defects, such as OVs and nanoholes, on the Co<sub>3</sub>O<sub>4</sub> catalyst for NitRR<sup>[61]</sup>. The defective Co<sub>3</sub>O<sub>4</sub>/Co with an interlaced nanosheet was synthesized through electrodeposition and calcination. The OVs improved the adsorption of NO<sub>3</sub><sup>-</sup> and increased active sites. The rich nanoholes displayed in Figure 5E may make additional channels for convenient mass transfer. As shown in Figure 5F, the adsorption energy of NO<sub>3</sub><sup>-</sup> on Co<sub>3</sub>O<sub>4</sub>-2Ov is lower than others at -1.81 eV. In addition, the energy barrier of HER on Co<sub>3</sub>O<sub>4</sub>-2Ov is the highest value of 1.15 eV [Figure 5G]. These results show that the OVs could enhance NO<sub>3</sub><sup>-</sup> adsorption and suppress HER. Figure 5H shows that Co<sub>3</sub>O<sub>4</sub>/Co-I has a higher yield rate of 4.43 mg h<sup>-1</sup> cm<sup>-2</sup> and FE of 88.7% than that of Co<sub>3</sub>O<sub>4</sub>/Co-h in 0.1 M Na<sub>2</sub>SO<sub>4</sub> with 1 mg mL<sup>-1</sup> of KNO<sub>3</sub> solution. Co<sub>3</sub>O<sub>4</sub>/Co exhibits a high performance in a flow electrolyzer system, with a yield rate of 8.96 mg h<sup>-1</sup> cm<sup>-2</sup> at 0.1 A cm<sup>-2</sup>. Research on 2D TMOs for NitRR is widespread due to their cost-effectiveness and stability. However, their inherent drawbacks, notably low conductivity and electrocatalyst activity, pose significant challenges. Addressing this, introducing defects in TMOs compensates for their intrinsic low conductivity. These defects overcome the conductivity issue and augment the electrochemical performance of catalysts by increasing both active area and activity. Consequently, defect engineering emerges as a promising solution to tackle the intrinsic problems of using oxides as electrocatalysts.

### Metal-organic frameworks

MOFs are new crystalline porous materials that can be formed by coupling metal ions/clusters with organic ligands<sup>[86]</sup>. They have been widely used in batteries<sup>[90]</sup>, supercapacitors<sup>[91]</sup>, catalysis<sup>[92]</sup>, *etc.*<sup>[93,94]</sup> due to their advantages such as high specific surface area<sup>[95]</sup>, tunable pore size, and high porosity<sup>[96]</sup>. The 2D nanosheets of MOFs have recently emerged as a promising material that makes them valuable in widespread electrocatalytic fields due to their atomic-level thickness, abundant active sites, and large surface area. Additionally, 2D MOF/COF nanosheet synthesis methods can be divided into top-down and bottom-up<sup>[97]</sup>. In the former, bulk crystals are synthesized first and then split into multi-layer or even single-layer nanosheets. The latter involves directly synthesizing 2D nanosheets by controlling the growth of bulk crystals in a specific direction. Bulk crystals connected between layers by hydrogen bonds or van der Waals forces are successfully exfoliated using ultrasound, mechanical force, *etc.* Due to the electrocatalytic reactions being related to the surface properties of the materials, 2D MOF materials provide an opportunity

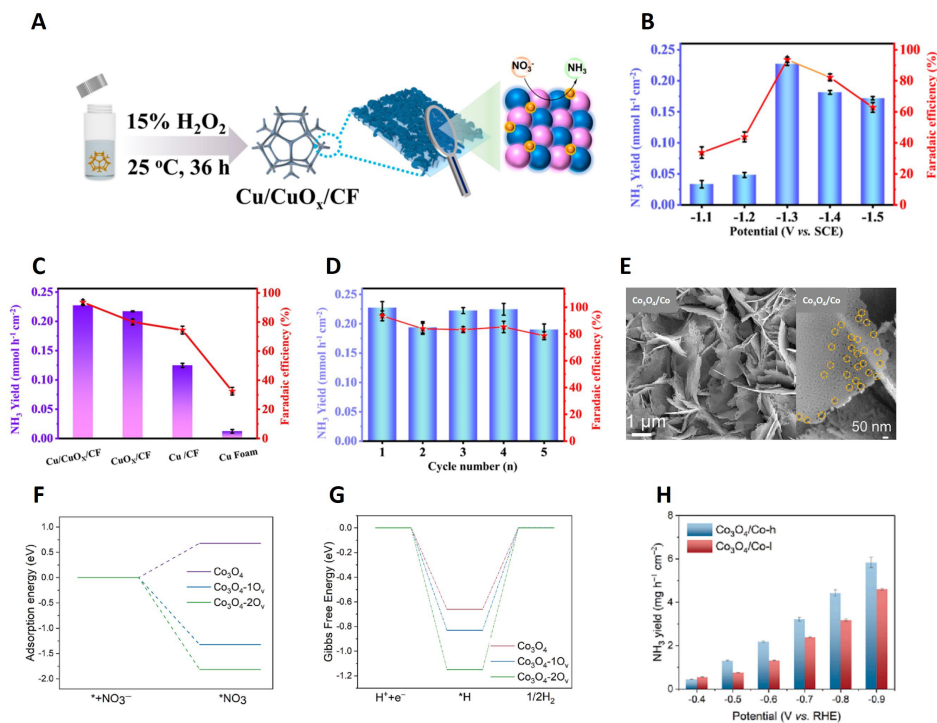


**Figure 5.** (A) Schematic image of the synthesis process for Cu/CuO<sub>x</sub>/CF. (B) NH<sub>3</sub> yield rates and FEs of Cu/CuO<sub>x</sub>/CF at different potentials. (C) NH<sub>3</sub> yield rates and FEs of Cu/CuO<sub>x</sub>/CF, CuO<sub>x</sub>/CF, Cu/CF, and CF. (D) The Cu/CuO<sub>x</sub>/CF recycling test was at -1.3 V (vs. SCE). (A-D) Figures are reprinted with permission from Ref.<sup>[60]</sup>. Copyright 2022 American Chemical Society<sup>[60]</sup>. (E) SEM images of Co<sub>3</sub>O<sub>4</sub>/Co-h. (F) Calculated adsorption energies of NO<sub>3</sub><sup>-</sup> on various Co<sub>3</sub>O<sub>4</sub> models. (G) Computed Gibbs free energies of H<sub>2</sub> production. (H) The NH<sub>3</sub> yield rate of Co<sub>3</sub>O<sub>4</sub>/Co-l and Co<sub>3</sub>O<sub>4</sub>/Co-h at different potentials. (E-H) Figures are reprinted with permission from Ref.<sup>[61]</sup>. Copyright 2023 Elsevier<sup>[61]</sup>.

to construct an efficient electrode with the advantages of flexible surface and active sites for electrocatalysis. In addition, the crystal structure of 2D MOF nanosheets provides highly exposed surface area and active sites at the atomic level. These consequences significantly shorten the diffusion lengths of the products and reactants to improve the performance of an electrocatalyst and have shown excellent performance in many fields. However, some traditional MOFs still suffer from low conductivity and stability.

Lv *et al.* reported 2D-In MOFs as an electrocatalyst with a uniformly dispersed single-atom site and enzyme mimic system for efficient NitRR<sup>[98]</sup>. The 2D-In MOFs were synthesized through a wet chemical method, and they showed a high ammonia yield rate of 278.8 μg h<sup>-1</sup> cm<sup>-2</sup> at -0.7 V (vs. RHE) and pH 2 with an optimal FE of 92%. These high performances are due to their stable microenvironment space and reversible ligand dissociation, as shown in Figure 6A. Figure 6B shows the solid-state cyclic voltammograms of 2D-In MOFs, showing two peaks of 0.22 and 0.55 V (vs. FC/FC<sup>+</sup>). Both peaks are attributed to redox-active tetrathiafulvalene (TTF) ligand and quasi-reversible electron transfer process. The reversible ligand dissociation at various potentials and pH is studied by *in situ* Raman spectroscopy in Figure 6C and D. The two peaks of 363 and 505 cm<sup>-1</sup> correspond to the In(III), and after the applied negative potential, two weak peaks of 438 and 806 cm<sup>-1</sup> appeared, which are due to In(II) and NO<sub>3</sub><sup>-</sup> adsorption at pH 1~3, respectively. On the other hand, apparent differences in peaks are not found in Figure 6D, which means the ligand dissociation mechanism does not work at the high pH. Lastly, the DFT method verifies the ligands' dynamic dissociation catalytic mechanism theoretically [Figure 6E].

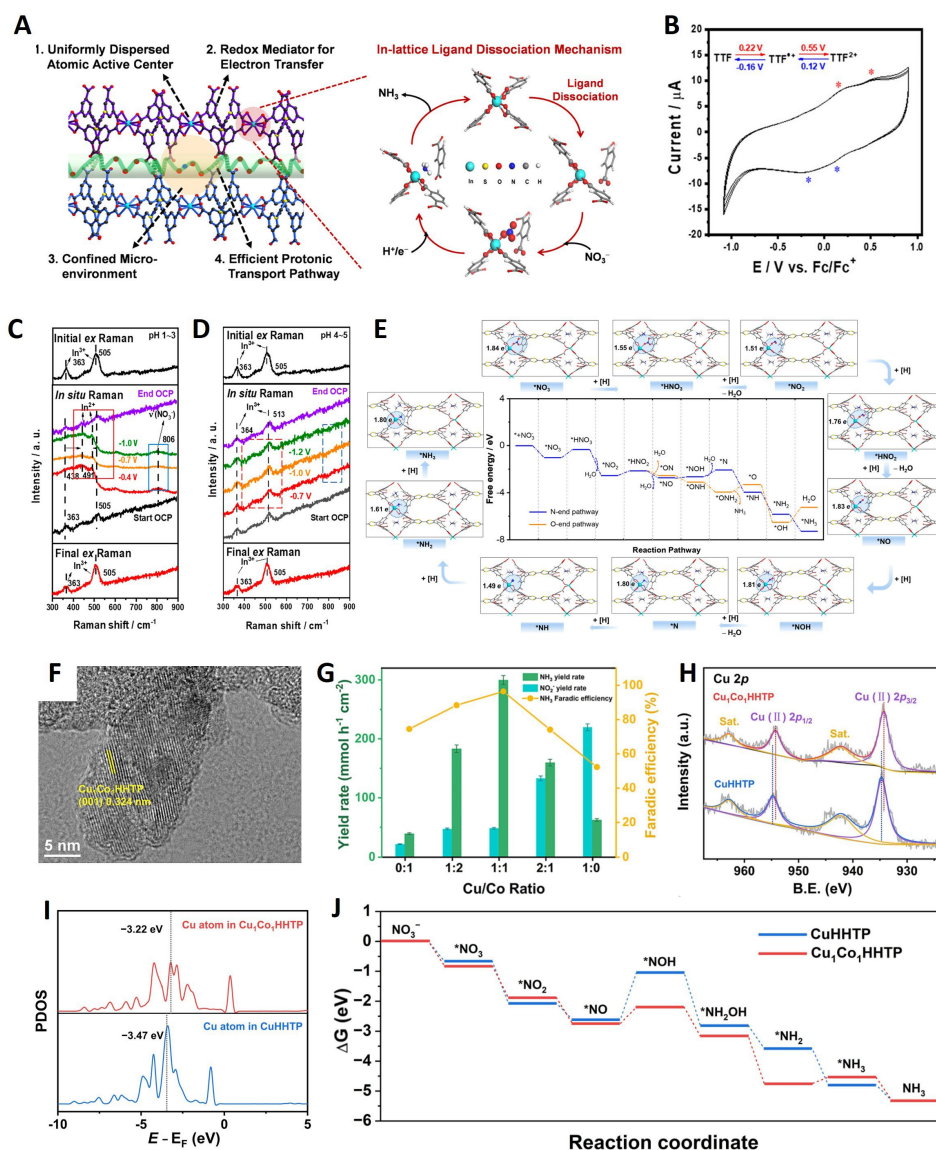


**Figure 6.** (A) Schematic illustration of the multifunctional motifs assembled in 2D-In-MOF and their functional characteristics and dynamic ligand dissociation mechanism. (B) Solid-state cyclic voltammograms of 2D-In-MOF conducted in 0.1 M  $\text{LiBF}_4$  in  $\text{CH}_3\text{CN}$  electrolyte. (C) *Ex situ* and *in situ* Raman spectra of 2D-In-MOF before (black) and after (red) electrocatalysis in  $\text{H}_2\text{SO}_4$  (pH = 1) with  $0.5 \text{ g L}^{-1} \text{ KNO}_3$  and (D) in  $50 \text{ mM H}_2\text{SO}_4$  (pH = 5) with  $0.5 \text{ g L}^{-1} \text{ KNO}_3$ . (E) Free energy diagram of electrochemical conversion of  $\text{NO}_3^-$  to  $\text{NH}_3$  for 2D-In-MOF and the optimized geometric structures of intermediates corresponding to the N-end pathway (pH = 2/3). (A-E) Figures are reprinted with permission from Ref.<sup>[98]</sup>. Copyright 2022 American Chemical Society<sup>[98]</sup>. (F) HR-TEM image of  $\text{Cu}_x\text{Co}_y\text{HHTP}$ , (G) The electrocatalytic activities of various  $\text{Cu}_x\text{Co}_y\text{HHTP}$  catalysts at -0.6 V (vs. RHE). (H) d-orbit PDOS of Cu site in  $\text{Cu}_x\text{Co}_y\text{HHTP}$  and  $\text{CuHHTP}$  slabs. (I) Free energy diagrams of the NitRR process on  $\text{Cu}_x\text{Co}_y\text{HHTP}$  and  $\text{CuHHTP}$  slabs. (F-J) Figures are reprinted with permission from Ref.<sup>[99]</sup>. Copyright 2023 Elsevier<sup>[99]</sup>.

Liu *et al.* reported bimetallic conductive copper-cobalt hexahydroxytriphenylene MOF ( $\text{Cu}_x\text{Co}_y\text{HHTP}$ ), which has a synergy effect between different single-metal sites and shows a great yield rate and a FE of  $299.9 \mu\text{mol h}^{-1} \text{ cm}^{-2}$  and 96.4%, respectively<sup>[99]</sup>.  $\text{Cu}_x\text{Co}_y\text{HHTP}$  was synthesized via the hydrothermal method, and the morphology was analyzed by High-Resolution Transmission Electron Microscopy (HR-TEM) [Figure 6F]. To investigate the synergistic effect of Co doping to Cu active sites, electrochemical NitRR with various Co/Cu ratios is performed. The  $\text{Cu}_1\text{Co}_1\text{HHTP}$  showed an optimal ratio of Cu:Co (1:1) with the highest ammonia yield rate and FE [Figure 6G]. After the doping of Co,  $\epsilon_d$  of the Cu site in  $\text{Cu}_1\text{Co}_1\text{HHTP}$

( $\epsilon_d = -3.22$  eV) is closer to the Fermi level than CuHHTP. This result explains that the doping of heteroatoms affects the electronic structure of Cu sites, which can adsorb the intermediate properly [Figure 6H]. Lastly,  $\text{Cu}_1\text{Co}_1\text{HHTP}$  is verified more favorable for NitRR from the Gibbs free-energy diagram, the  $\Delta G$  of  $\text{NO}_3^-$  adsorption and potential determining step (PDS) ( $\text{NO}^* \rightarrow \text{NOH}^*$ ) on the Cu site of  $\text{Cu}_1\text{Co}_1\text{HHTP}$  are  $-0.82$  and  $0.54$  eV, respectively, which are lower than CuHHTP ( $-0.55$  and  $1.56$  eV) [Figure 6I and J].

Fang *et al.* reported 2D-Fe cyano NSs (nanosheets) as multi-functional electrocatalysts that have abundant  $\text{Fe}^0$  active sites for NitRR and oxygen evolution reaction (OER) via topotactic conversion and electro-reduction [Figure 7A]<sup>[100]</sup>. As shown in Figure 7B, Fe cyano NSs have a large active surface area, which is 1.54 times the Fe-cyano bulk and super hydrophilic properties from electrical double-layer capacitance (EDLC) and contact angle data. These properties are due to 2D engineering and hydrophilic functional groups and are favorable for electrode contact with electrolytes and  $\text{NO}_3^-$  adsorption. In addition, the X-ray Photoelectron Spectroscopy (XPS) data shows the generation of  $\text{Fe}^0$  in Fe cyano NSs after the electro-reduction process, and the  $\text{Fe}^0$  sites are verified as active sites for NitRR by poisoning Fe sites using potassium thiocyanide (KSCN) [Figure 7C and D]. DFT simulation shows negative  $\Delta G$  of  $\text{NO}_3^-$  adsorption on  $\text{Fe}^0$  sites that supports the suppression of HER and NitRR selectivity. In the electrochemical NitRR test, the Fe cyano NSs exhibit a high ammonia yield rate of  $42.1 \text{ mg h}^{-1} \text{ mg}_{\text{cat.}}^{-1}$  and an FE of over 90% at  $-0.5 \text{ V}$  (vs. RHE) [Figure 7E]. Furthermore, Fe cyano NS-based material as a multifunctional catalyst showed excellent durability without degradation of cell voltage at  $60 \text{ mA cm}^{-2}$  for an electrolyzer of OER and NitRR [Figure 7F]. Therefore, recent research on 2D-MOFs as electrocatalysts has progressed due to their high surface area and shortened diffusion lengths. In particular, 2D-MOFs, which have uniformly dispersed single atom sites and doped single heteroatom sites, show a synergistic effect on electrochemical activity and can improve conductivity and stability with reversible reactions.

### MXenes

MXenes are generally defined as 2D TM carbides or nitrides, with  $\text{Ti}_3\text{C}_2\text{T}_x$  synthesized from the  $\text{M}_{n+1}\text{AX}_n$  (MAX) phase of  $\text{Ti}_3\text{AlC}_2$  first reported in 2011<sup>[101]</sup>. The thickness of MXenes is typically in the 1 nm range and depends on the  $n$  value ( $\text{M}_{n+1}\text{X}_n\text{T}_x$ ) of the MXenes<sup>[102]</sup>. MXenes are primarily synthesized by selectively etching the A layer from the precursor MAX phase, which is a precursor of MXenes and is typically a series of ternary layer compounds, where M is a TM, A is an element of group IIIA or IVA in the periodic table, and X is carbon or nitrogen [Figure 8A]<sup>[103]</sup>. Because the M-X covalent bonds and M-A metal bonds on MAX are powerful, for breaking the M-A bonds, potent etching agents such as hydrofluoric acid (HF) and lithium fluoride-hydrochloric acid mixtures (LiF-HCl) are required. As a result, the surface of MXenes is terminated with abundant functional groups such as  $-\text{OH}$  and  $-\text{O}$ , which vary in type and amount depending on the etching route [Figure 8B]<sup>[104]</sup>. Various stoichiometries of MXenes have been studied, such as monometallic MXenes, bimetallic MXenes, and multi-metal MXenes [Figure 8C]<sup>[105]</sup>.

Due to their numerous properties, including unique mechanical properties<sup>[106]</sup>, metallic conductivity<sup>[107]</sup>, in-plane anisotropic structure<sup>[108]</sup>, and tunable band gap<sup>[109]</sup>, MXenes have been arising as multipurpose 2D materials for promising applications<sup>[110-112]</sup>. Compared to other 2D materials, they have abundant terminal functional groups<sup>[113]</sup>, enabling reversible redox reactions<sup>[114]</sup>. Unlike other 2D materials, they do not require processing to increase the exposure and density of active sites. In general, MXene basal planes are considered catalytically inactive<sup>[115]</sup>. However, these can become active by tuning their terminal groups. Hu *et al.* reveal the mechanism of  $\text{NO}_3^-$  to ammonia on  $\text{M}_3\text{C}_2$  MXenes, and their catalytic activity depends on the terminated group, OV, and environment of different pH via DFT calculations<sup>[116]</sup>. Generally, most  $\text{M}_3\text{C}_2$  MXenes prefer HER selective; on the other hand, O-terminated  $\text{Ti}_3\text{C}_2$  and  $\text{Ti}_3\text{C}_2\text{O}_2$  with OV groups have NitRR selectivity due to the electronic state of N intermediate on  $\text{Ti}_3\text{C}_2\text{O}_2$  with OV showed closer than

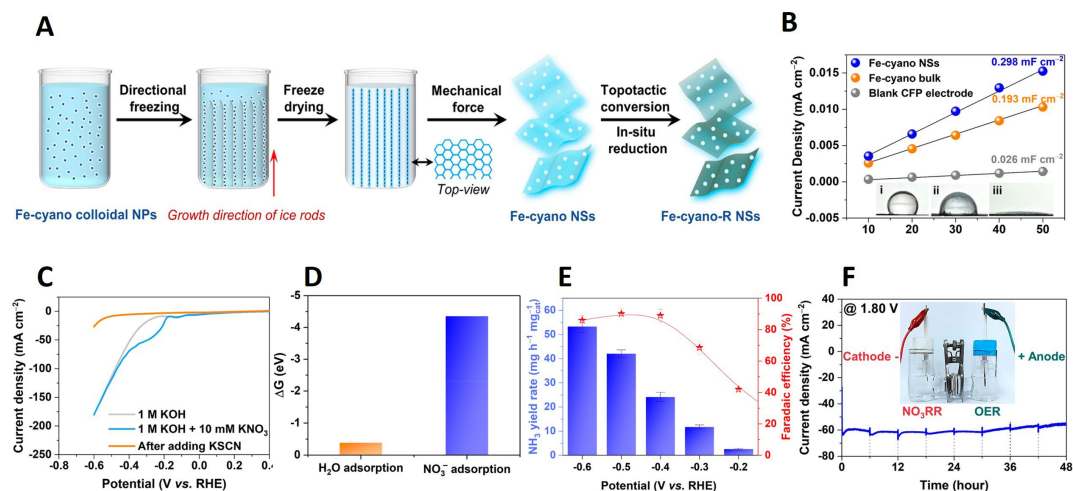


**Figure 7.** (A) Synthesis of ultra-large Fe-cyano NSs via directional freezing. (B) EDLC of blank CFP electrode, Fe-cyano bulk, and NS electrocatalysts. Inset of (B) CAs of (i) blank CFP electrode, (ii) Fe-cyano bulk, and (iii) NS electrocatalysts. (C) Poisoning experiment on Fe-cyano-R NSs. (D)  $\text{H}_2\text{O}$  and  $\text{NO}_3^-$  adsorption on  $\text{Fe}^0$ . (E) Ammonia yield rate and Faradaic efficiency (FE) at various potentials on Fe-cyano NSs. (F) Stability of electrolyzer. Reprinted with permission from Ref. <sup>[100]</sup>. Copyright 2022 American Chemical Society <sup>[100]</sup>.

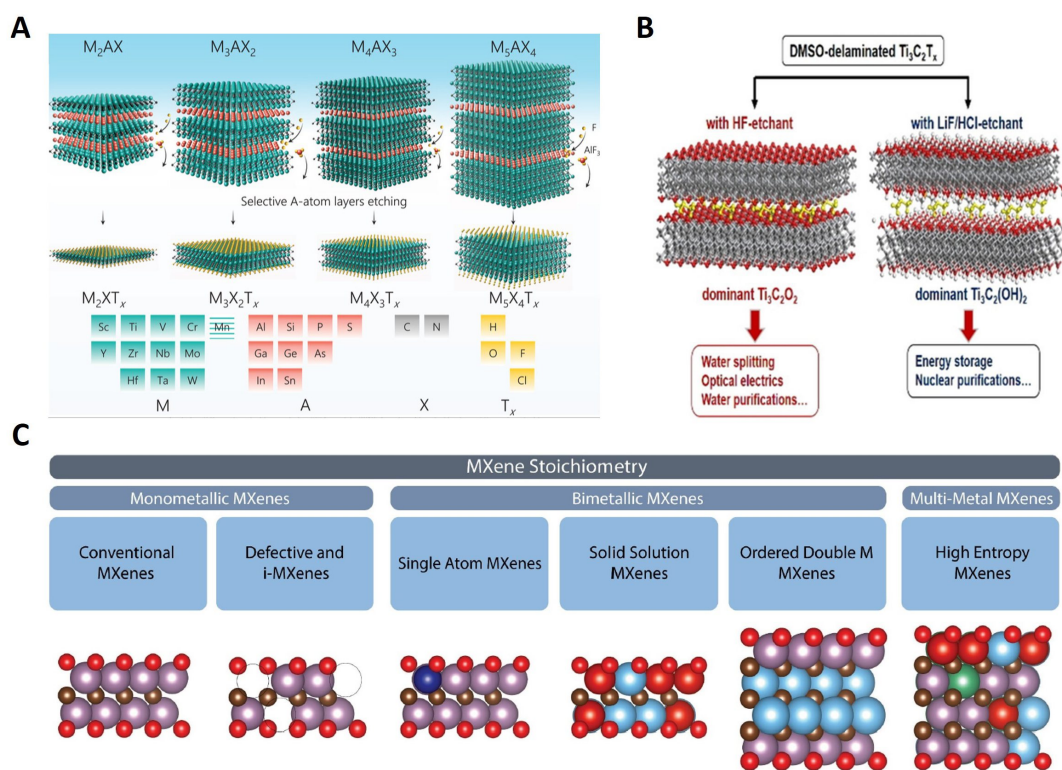


**Figure 8.** (A) A schematic representation of MAX structures from  $n = 1$  to  $n = 4$  and their etched MXene structures. Reprinted with permission from Ref. <sup>[103]</sup>. Copyright 2021 Wiley-VCH <sup>[103]</sup>. (B) A schematic of different surface functional groups depending on the etching route. Reprinted with permission from Ref. <sup>[104]</sup>. Copyright 2018 Wiley-VCH <sup>[104]</sup>. (C) Schematic depicting different MXene stoichiometries. Reprinted with permission from Ref. <sup>[105]</sup>. Copyright 2023 Wiley-VCH <sup>[105]</sup>.

$\text{Ti}_3\text{C}_2$  to the Fermi level. These results are due to the increased oxidation state of surface Ti, which weakens  $\text{NH}_x$  adsorption and facilitates the hydrogenation process.

Cai *et al.* reported that surface hydroxyl on oxygen-functionalized  $\text{Ti}_3\text{C}_2$  MXene (Of-TiMX) plays a vital role in the NitRR process<sup>[115]</sup>. The Of-TiMX was synthesized via three steps of etching, exfoliation, and calcination to make an oxygen group on the surface of TiMX [Figure 9A]. The Of-TiMX shows not only selective NitRR but also a high FE and an ammonia yield rate of 90.4% and  $0.99 \text{ mg h}^{-1} \text{ cm}^{-2}$  at  $-1.7 \text{ V}$  (*vs.* SCE), which indicates HER is effectively suppressed on its surface [Figure 9B].

From the surface Pourbaix diagram, the trend of the amount of surface hydroxyl grows as the potential increases [Figure 9C]. This trend is related to the experimental results that the Of-TiMX has the highest NitRR performance at  $-1.7 \text{ V}$  (*vs.* SCE) because the hydroxyl groups allow interfacial H-bonding with  $\text{NO}_3^-$  and other intermediates for  $\text{NH}_3$  production. In addition, the free energy diagram for NitRR on the hydroxyl-covered surface of Of-TiMX suggests the NitRR pathway to synthesize ammonia and support high optimized potential and selectivity [Figure 9D]. Hence, recent research on MXenes and advances in computational science have been extensive. Significantly, the surface modification of MXenes, which have abundant and tuneable functional groups on their surface, is determined to improve electrocatalytic activity and selectivity with a high ammonia yield rate.

### Graphene-based materials

To reduce the use of precious metals, carbon nanomaterials are commonly used in electrocatalytic applications due to their high electrical conductivity, low cost, and chemical stability<sup>[117]</sup>. Graphene, one of the carbon nanomaterials, has mainly been utilized as a catalyst or support to improve the electrocatalytic performance of the NitRR owing to its 2D structure. However, when used alone, graphene has relatively poor electrocatalytic properties, such as low activity and selectivity. Various engineering approaches have been investigated to overcome these problems, including a combination of TMs and defect engineering.

Graphene has been widely used as a support for single-atom catalysts (SACs) due to its suitability as an excellent structural support. SACs are dispersed or coordinated atomically on the surface of 2D materials such as graphene, and surface defects are often utilized as their active sites. These catalysts have many advantages, including high stability, activity, selectivity, efficient active sites, and drastic cost reduction. Additionally, they allow for the tuning of the selectivity and activity of electrocatalytic reactions<sup>[118]</sup>. To synthesize the SACs, lots of synthesis methods, such as wet-chemical, MOF-derived, atomic layer deposition (ALD), co-precipitation, and impregnation, have been investigated<sup>[119]</sup>.

Wu *et al.* synthesized Fe SAC anchored on graphene through pyrolysis and etching, as shown in Figure 10A<sup>[62]</sup>. The Fe SAC on graphene exhibits higher electrocatalytic performance with a yield rate of  $\sim 20,000 \text{ } \mu\text{g h}^{-1} \text{ mg}_{\text{cat}}^{-1}$  at  $-0.85 \text{ V}$  (*vs.* RHE) and a FE of  $\sim 75\%$  at  $-0.66 \text{ V}$  (*vs.* RHE) than those of iron nanoparticles supported on nitrogen-doped carbon (FeNP/NC) and NC [Figure 10B and C]. The N-N coupling pathway for  $\text{N}_2$  production, one of the competitive reactions, can be inhibited due to the isolated active Fe atoms, as the  $^*\text{N}$  on neighboring active sites cannot exist side by side. Figure 10D displays the minimum energy pathway (MEP) of NitRR on the Fe single atom site. DFT calculations show that the MEP converts to a downhill conformation when  $U = -0.3 \text{ V}$  (*vs.* RHE) (black line) in Figure 10E; the results support that the experimental onset potential [ $\sim -0.4 \text{ V}$  (*vs.* RHE)] is reasonable.

Beyond the study of SACs, dual-atom catalysts (DACs) have been investigated because of their unique structure. Their structure could suppress HER on their surface and increase the selectivity of NitRR due to an ensemble effect<sup>[120]</sup>. Zhao *et al.* calculated the DFT of DACs embedded in N-graphene for NitRR and demonstrated the results with subsequent experiments<sup>[121]</sup>. The geometric structure of DACs is determined by the d-band type of the constituent metals [Figure 10F and G]. The DFT indicated the synergistic effects

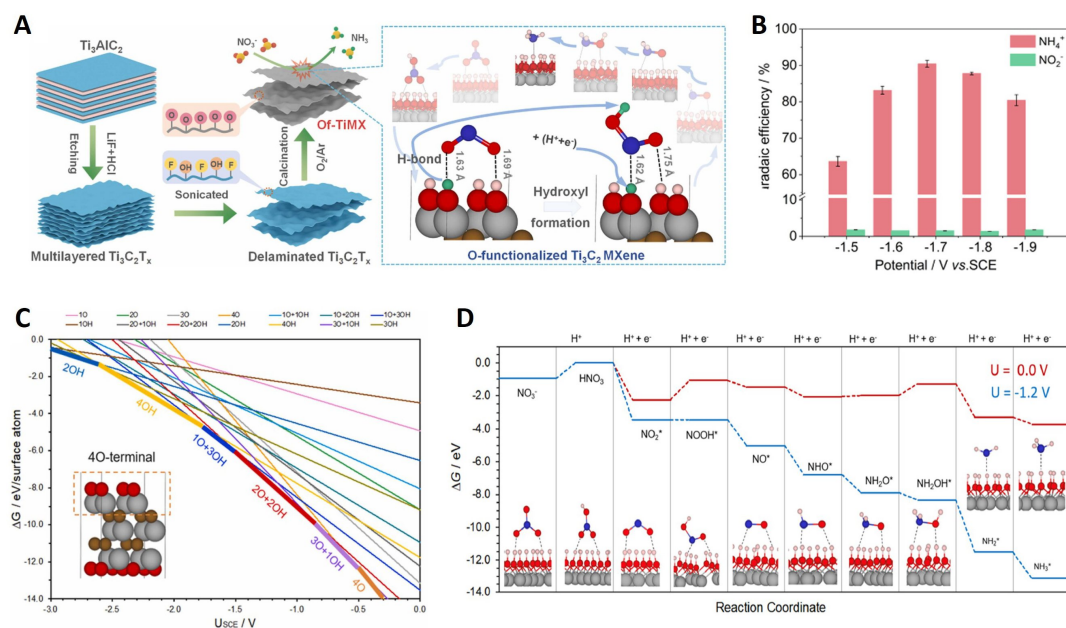


**Figure 9.** (A) Schematic illustration of synthesizing the Of-TiMX for NitRR. (B) FEs of ammonia and nitrite of Of-TiMX at different potentials. (C) Pourbaix diagrams for Of-TiMX at pH 7. (D) Free-energy diagrams for NitRR on the surface of full OH-terminated Of-TiMX at  $U = 0.0$  V and  $U = -1.2$  V (vs. SHE). Reprinted with permission from Ref. [115]. Copyright 2023 Elsevier [115].

of two active sites improve the activation of catalysts, which is related to intrinsic d-band centers of active sites. Then, it is revealed that  $\text{Cu}_2@N_3-6$  catalysts have high electrocatalytic performance for NitRR in DFT results, and  $\text{Cu}_2@N_3-6$  achieved a high FE of 97.4% and yield rate of  $18.2 \text{ mg h}^{-1} \text{ cm}^{-2}$  at  $-0.8$  V (vs. RHE) in the experiment [Figure 10H].

Defect engineering can increase the electrochemical activity of the graphene for the NitRR due to the change in electronic structures. Huang *et al.* show a skyscraping FE of nearly 100% with amorphous graphene for NitRR [122]. The amorphous graphene was synthesized via laser induction, which resulted in numerous defects, disordered pentagons, hexagons, and heptagons in graphene, and Figure 10I shows these defects in graphene. These defects increase the selectivity of the graphene for NitRR. The amorphous graphene has high electrocatalytic performances, which are FE of about 100% and  $\text{NH}_3$  production of  $2,859 \mu\text{g h}^{-1} \text{ cm}^{-2}$  at  $-0.93$  V (vs. RHE) [Figure 10J and K]. As mentioned above, graphene-based materials have gained attention as catalysts and support for NitRR due to their high conductivity, cost-efficiency, and expansive surface area, reducing the reliance on precious catalysts while maintaining electrochemical performance. Recently, studies have explored the potential of graphene as a standalone catalyst for NitRR, particularly when coupled with defect engineering. However, some defect engineering, such as N-S or N-P co-doping on graphene, remains unapplied for NitRR. Additionally, other carbon-based materials, such as carbon nanotubes (CNTs), with defect engineering have not received extensive investigation, suggesting that carbon-based materials hold further potential for NitRR.

## CONCLUSIONS AND PERSPECTIVES

Electrochemical synthesis of green ammonia has been focused on as an alternative way to the energy-intensive Haber-Bosch process due to its advantages, such as zero-carbon emission, scalability, and production under ambient conditions. However, commercialization of NitRR undergoes inevitable drawbacks, such as low selectivity of ammonia and high cost of electrocatalysts, due to immature

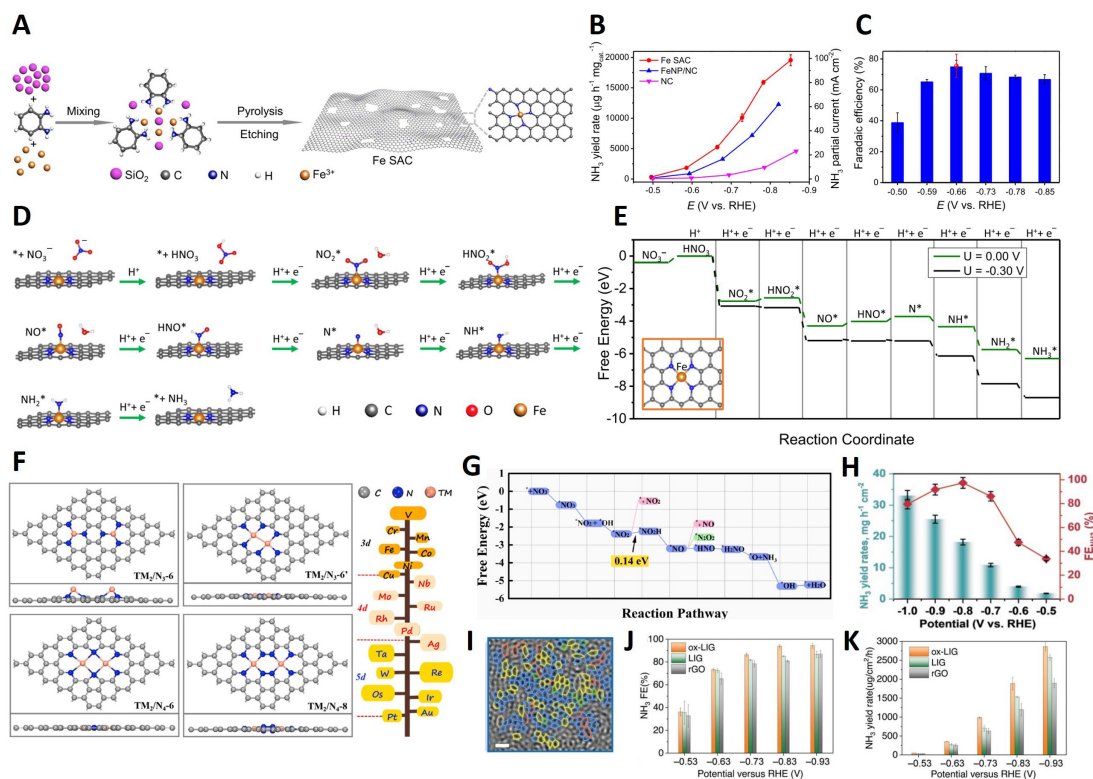


**Figure 10.** (A) Schematic image of the synthesis process for Fe SAC. (B) NH<sub>3</sub> partial current density and yield rate of Fe SAC, FeNP/NC, NC. (C) NH<sub>3</sub> FE of Fe SAC at different potentials. (D) Calculated minimum energy pathway on Fe SAC for NitRR. (E) Calculated accessible energy pathway at U = 0 and -0.3 V (vs. RHE). (A-E) Figures are reprinted with permission from Ref.<sup>[62]</sup>. Copyright 2021 Springer Nature Limited<sup>[62]</sup>. (F) The metal atoms and substrates considered for constructing the DACs on N-graphenes. (G) Calculated free energy of NitRR on Cu<sub>2</sub>/N<sub>3</sub>-6 and the involved intermediates. (H) Potential-dependent NH<sub>3</sub> yield rate and FE of Cu<sub>2</sub>/N<sub>3</sub>-6. (F-H) Figures are reprinted with permission from Ref.<sup>[121]</sup>. Copyright 2023 Elsevier.<sup>[121]</sup>. (I) HR-TEM image of ox-LIG. (J) NH<sub>3</sub> FE and (K) ox-LIG, LIG, and rGO yield rates at different potentials. (I-K) Figures are reprinted with permission from Ref.<sup>[122]</sup>. Copyright 2023 Wiley-VCH GmbH<sup>[122]</sup>.

technology and competitive HER. To increase the electrochemical performance of the NitRR, the design strategies of electrocatalysts have been studied over the past decade. Furthermore, 2D structured materials have been investigated as promising candidates for efficient electrocatalysts due to their advantages, such as a particular surface area with an abundant active site, ease of modification, and low cost. In addition, various defect engineering, such as oxygen defect, doping, and topological defects, have been considered to improve the electrocatalytic performance because these defects in 2D electrocatalysts not only increase the mass/charge transport, active site, and electrical conductivity but can also tune the electronic structure.

This review summarized the recent advances and development of 2D catalysts with defect engineering for NitRR. While some 2D materials are employed as catalysts for NitRR, certain drawbacks become apparent. For example, TMOs exhibit low conductivity, and graphene demonstrates low activity. However, defects emerge as a solution, addressing these intrinsic issues by enhancing catalyst conductivity and activity. Unexplored 2D materials, such as TaS<sub>2</sub>, MoTe<sub>2</sub>, and defect-rich CNTs, remain untapped for converting from nitrate to ammonia. Additionally, various defect engineering techniques, such as N-P or N-S co-doping and topological defects, await NitRR exploration. Consequently, the remaining candidates can potentially increase ammonia yield and FE.

**Table 2. Comparison of different 2D-structured materials as electrocatalysts for NitRR**

Category	Electrocatalysts	Synthesis method	Substrate	Electrolyte	NH <sub>3</sub> yield rate	FE (%)	Selectivity (%)	Ref.
Layered double hydroxide (LDH)	CoFe LDH	Hydrothermal	Ni foam	1 M KOH + 1,400 ppm KNO <sub>3</sub>	0.93 mmol h <sup>-1</sup> cm <sup>-2</sup> @-0.45 V (vs. RHE)	97.68	98.93	[52]
	Ni <sub>3</sub> Fe-CO <sub>3</sub> LDH	Co-precipitation	Cu foam	1 M KOH + 5 mM KNO <sub>3</sub>	1.261 mg h <sup>-1</sup> cm <sup>-2</sup> @-0.2 V (vs. RHE)	96.80	95.80	[53]
Chalcogenide	Fe-MoS <sub>2</sub>	Hydrothermal	Carbon cloth	0.1 M Na <sub>2</sub> SO <sub>4</sub> + 0.1 M NaOH + 0.1 M NaNO <sub>3</sub>	0.03 mmol h <sup>-1</sup> cm <sup>-2</sup> @-0.5 V (vs. RHE)	98		[54]
	Fe-MoS <sub>2</sub>	Hydrothermal	Carbon cloth	1 M LiCl + 0.25 M LiNO <sub>3</sub>	9.75 mg h <sup>-1</sup> cm <sup>-2</sup> @-0.85 V (vs. RHE)	90		[83]
	Cu-SnS <sub>2-x</sub>	Solvothermal	Carbon cloth	0.1 M KOH + 0.1 M KNO <sub>3</sub>	0.63 mmol h <sup>-1</sup> mg <sub>cat.</sub> <sup>-1</sup> @-0.7 V (vs. RHE)	93.80		[55]
	B-MoS <sub>2</sub>	Hydrothermal	Carbon cloth	0.5 M Na <sub>2</sub> SO <sub>4</sub> + 0.1 M NaNO <sub>3</sub>	10.8 mg h <sup>-1</sup> cm <sup>-2</sup> @-0.7 V (vs. RHE)	92.30		[123]
Transition-metal oxide (TMO)	Co <sub>3</sub> O <sub>4</sub> /Co-I	Electrodeposition & calcination	Co foam	1,000 ppm NO <sub>3</sub> <sup>-</sup> + 0.1 M Na <sub>2</sub> SO <sub>4</sub>	4.43 mg h <sup>-1</sup> cm <sup>-2</sup> @-0.8 V (vs. RHE)	88.70	83.30	[61]
	Cu/CuO <sub>x</sub> /CF	Oxidation treatment	Cu foam	0.5 M K <sub>2</sub> SO <sub>4</sub> + 200 mg L <sup>-1</sup> NO <sub>3</sub> <sup>-</sup>	0.23 mmol h <sup>-1</sup> cm <sup>-2</sup> @-1.3 V (vs. SCE)	93.58	95.00	[60]
	CuO NWAs@Fe <sub>3</sub> O <sub>4</sub>	Hydrolysis & pyrolysis	Cu foam	1 M KOH + 1,400 ppm NO <sub>3</sub> <sup>-</sup>	1.691 mmol h <sup>-1</sup> cm <sup>-2</sup> @-0.27 V (vs. RHE)	99.46	88.68	[124]
Metal-organic framework (MOF)	Ni-MOF	Solvothermal	Ni foam	70 mg·L <sup>-1</sup> NaNO <sub>3</sub> , 0.1 M Na <sub>2</sub> SO <sub>4</sub>	110.13 ug h <sup>-1</sup> cm <sup>-2</sup> @-1.4 V (vs. SCE)	96.40	80	[58]
	cMOF(Cu <sub>x</sub> Co <sub>y</sub> HHTP)	Hydrothermal	Carbon cloth	0.5 M Na <sub>2</sub> SO <sub>4</sub> + 0.1 M NaNO <sub>3</sub>	299.9 μmol h <sup>-1</sup> cm <sup>-2</sup> @-0.6 V (vs. RHE)	96.40		[99]
	Fe-cyano NSs	Sol-gel	Carbon fiber paper	0.1 M KNO <sub>3</sub> + 1 M KOH	42.1 mg h <sup>-1</sup> mg <sub>cat.</sub> <sup>-1</sup> @-0.5 V (vs. RHE)	90.20		[100]
	In-MOF In8	Solvothermal	Carbon paper	5 mM H <sub>2</sub> SO <sub>4</sub> + 15 g·L <sup>-1</sup> KNO <sub>3</sub>	256.9 μg h <sup>-1</sup> mg <sub>cat.</sub> <sup>-1</sup> @-0.7 V (vs. RHE)	90.10	99.30	[98]
MXene	Ti <sub>3</sub> C <sub>2</sub>	Etching & ultrasonication	Carbon paper	0.5 M K <sub>2</sub> SO <sub>4</sub> + 200 ppm KNO <sub>3</sub>	0.99 mg h <sup>-1</sup> cm <sup>-2</sup> @-1.7 V (vs. SCE)	90		[115]
	BP/Nb <sub>2</sub> C	Self-assembly	Carbon cloth	0.1 M K <sub>2</sub> SO <sub>4</sub> + 0.05 M KNO <sub>3</sub>	1,967.0 μg h <sup>-1</sup> cm <sup>-2</sup> @-0.6 V (vs. RHE)	90.4	@-0.5 V vs. RHE	[125]
	Bi <sub>2</sub> O <sub>3</sub> /MXene	Solvothermal	Carbon paper	1,000 ppm NO <sub>3</sub> <sup>-</sup> + 0.5 M Na <sub>2</sub> SO <sub>4</sub>	7.00 mg h <sup>-1</sup> cm <sup>-2</sup> @-1.8 V (vs. SCE)	91.10		[126]
	Fe <sub>1</sub> Cu <sub>2</sub> @MXene	Wet-chemical	Carbon cloth	100 mg L <sup>-1</sup> KNO <sub>3</sub> + 0.1 M Na <sub>2</sub> SO <sub>4</sub>	1.2 mg h <sup>-1</sup> cm <sup>-2</sup> @-0.95 V (vs. RHE)	52	99.60	[127]
	FeNPs@MXene	Wet-chemical	Carbon cloth	100 mg L <sup>-1</sup> NO <sub>3</sub> + 0.5 M Na <sub>2</sub> SO <sub>4</sub>	-0.8 mg h <sup>-1</sup> cm <sup>-2</sup> @-0.95 V (vs. RHE)	20.00	76.80	[128]
	CuCl <sub>2</sub> -BEF	Wet-chemical	Carbon cloth	100 mg L <sup>-1</sup> NO <sub>3</sub> + 0.5 M Na <sub>2</sub> SO <sub>4</sub>	1.82 mg h <sup>-1</sup> cm <sup>-2</sup>	44.70	98.60	[129]

Graphene-basedmaterial	Mo <sub>2</sub> C NSs	Carbonization	Carbon paper	1 M NaOH + 0.1 M NaNO <sub>3</sub>	@-1.0 V (vs. RHE) 25.2 mg h <sup>-1</sup> mg <sub>cat.</sub> <sup>-1</sup> @-0.4 V (vs. RHE)	81.4 @-0.3 V vs. RHE		[130]
	Fe SAC	Wet-chemical	Glassy carbon	0.1 M K <sub>2</sub> SO <sub>4</sub> + 0.5 M KNO <sub>3</sub>	20,000 ug h <sup>-1</sup> mg <sub>cat.</sub> <sup>-1</sup> @-0.85 V (vs. RHE)	75 @-0.66 V vs. RHE	69	[62]
	Cu <sub>2</sub> @N <sub>3</sub> -6	Pyrolysis method	Carbon cloth	0.5 M Na <sub>2</sub> SO <sub>4</sub> + 0.1 M NaNO <sub>3</sub>	18.2 mg h <sup>-1</sup> cm <sup>-2</sup> @-0.8 V (vs. RHE)	97.40		[121]
	ox-LIG	Laser induction	Cellulose paper/Au layer	1 M NaNO <sub>3</sub>	2,859 μg h <sup>-1</sup> cm <sup>-2</sup> @-0.93 V (vs. RHE)	96.40	> 70	[122]

Recent studies demonstrated the high electrocatalytic performance of NitRR, as shown in Table 2. Understanding the NitRR mechanism on the catalyst is essential to improve electrocatalytic performance. In previous studies, the NitRR mechanism of defects-containing 2D catalysts has also been investigated by the DFT method. However, most DFT calculations have focused on point defects, such as vacancies and doping. There are still unresolved issues related to NitRR regarding complex 2D and 3D defects, such as grain boundaries (GBs), twins, distortion, voids, and cracks. In realistic situations, catalysts have numerous GBs, and the unsaturated coordination of GB atoms can enhance catalytic activity. DFT calculations can utilize two GB bulk models built based on the coincidence site lattice (CSL) theory to address this. Moreover, appropriate conditions are also necessary for understanding the precise properties of each type of defect.

Understanding fluid dynamics within the flow electrolyzer is a critical concern in the scale-up process. These considerations become particularly vital as cell designs progress from H-type cells to flow cells for NitRR. Understanding NitRR in the flow state is paramount. Various approaches can be employed to achieve a comprehensive understanding of NitRR in a flow state, including computational simulations such as computational fluid dynamics (CFD) and molecular dynamics (MD). Additionally, *in situ* characterization techniques, such as *in situ* Fourier-transform infrared spectroscopy (FT-IR), *in situ* Raman spectroscopy, *in situ* X-ray absorption spectroscopy (XAS), *in situ* scanning electrochemical microscopy (SECM), and online DEMS, need further exploration to accurately decipher the conversion of NO<sub>3</sub><sup>-</sup> to NH<sub>3</sub> accurately and to gain insights into the kinetics of the reaction. These *in situ* measurements will provide clues to suppress the production of by-products such as H<sub>2</sub>, N<sub>2</sub>, and NO<sub>2</sub><sup>-</sup>. Although some challenges remain, progress is highly expected through continuous research. This review will help bridge the gap between theory and experiment to understand 2D materials and defect engineering for NitRR.

## DECLARATIONS

### Author's contributions

Conceptualization, investigation, visualization, validation, writing - original draft, writing - review & editing: Choi J, Im S, Kim JK, Sim U

Investigation, visualization, writing - review & editing: Choi J

Validation, writing - review & editing: Surendran S

Writing - review & editing: Moon DJ, Kim JY

#### Availability of data and materials

Not applicable.

#### Financial support and sponsorship

This work was supported by the Korea Institute of Energy Technology Evaluation and Planning (KETEP) grant funded by the Korean government (MOTIE) (No. RS-2023-00242227 (Clean Hydrogen and Ammonia Innovation Research Center) and No. 20224000000320). This work was supported from the National Research Foundation of Korea (NRF) grant funded by the Korean government (MSIT) (No. 2022R1A2C1012419). This work was supported by the New & Renewable Energy Core Technology Program of the Korea Institute of Energy Technology Evaluation and Planning (KETEP) granted financial resource from the Ministry of Trade, Industry & Energy, Republic of Korea (No. 20213030040590). This research was supported by Nano-Material Technology Development Program through the National Research Foundation of Korea (NRF) funded by Ministry of Science and ICT (2020M3H4A3106313). Additionally, this work was backed by the KENTECH Research Grant funded by the Korea Institute of Energy Technology, Republic of Korea (KRG2022-01-016). This research also benefited from the "Regional Innovation Strategy (RIS)" through the National Research Foundation of Korea (NRF), funded by the Ministry of Education (MOE) (2021RIS-002).

#### Conflicts of interest

All authors declared that there are no conflicts of interest.

#### Ethical approval and consent to participate

Not applicable.

#### Consent for publication

Not applicable.

#### Copyright

© The Author(s) 2024.

#### REFERENCES

1. Klerke A, Christensen CH, Nørskov JK, Vegge T. Ammonia for hydrogen storage: challenges and opportunities. *J Mater Chem* 2008;18:2304-10. [DOI](#)
2. Wang Y, Zhou X, Liu L. Theoretical investigation of the combustion performance of ammonia/hydrogen mixtures on a marine diesel engine. *Int J Hydrog Energy* 2021;46:14805-12. [DOI](#)
3. Chehade G, Dincer I. Progress in green ammonia production as potential carbon-free fuel. *Fuel* 2021;299:120845. [DOI](#)
4. Guo Y, Pan Z, An L. Carbon-free sustainable energy technology: direct ammonia fuel cells. *J Power Sources* 2020;476:228454. [DOI](#)
5. Valera-Medina A, Xiao H, Owen-Jones M, David W, Bowen P. Ammonia for power. *Prog Energy Combust Sci* 2018;69:63-102. [DOI](#)
6. Cheng S, Logan BE. Ammonia treatment of carbon cloth anodes to enhance power generation of microbial fuel cells. *Electrochem Commun* 2007;9:492-6. [DOI](#)
7. Giddey S, Badwal SPS, Munnings C, Dolan M. Ammonia as a renewable energy transportation media. *ACS Sustain Chem Eng* 2017;5:10231-9. [DOI](#)
8. Wang W, Herrerros JM, Tsolakis A, York AP. Ammonia as hydrogen carrier for transportation; investigation of the ammonia exhaust gas fuel reforming. *Int J Hydrog Energy* 2013;38:9907-17. [DOI](#)
9. Fu E, Gong F, Wang S, Xiao R. Chemical looping technology in mild-condition ammonia production: a comprehensive review and analysis. *Small* 2024;20:e2305095. [DOI](#)
10. Erisman JW, Sutton MA, Galloway J, Klimont Z, Winiwarter W. How a century of ammonia synthesis changed the world. *Nature Geosci* 2008;1:636-9. [DOI](#)

11. Gao Y, Wang R, Li Y, et al. Regulating dynamic equilibrium of active hydrogen for super-efficient nitrate electroreduction to ammonia. *Chem Eng J* 2023;474:145546. DOI
12. Yang B, Ding W, Zhang H, Zhang S. Recent progress in electrochemical synthesis of ammonia from nitrogen: strategies to improve the catalytic activity and selectivity. *Energy Environ Sci* 2021;14:672-87. DOI
13. Noh H, Kang K, Seo Y. Environmental and energy efficiency assessments of offshore hydrogen supply chains utilizing compressed gaseous hydrogen, liquefied hydrogen, liquid organic hydrogen carriers and ammonia. *Int J Hydrog Energy* 2023;48:7515-32. DOI
14. Asif M, Sidra Bibi S, Ahmed S, et al. Recent advances in green hydrogen production, storage and commercial-scale use via catalytic ammonia cracking. *Chem Eng J* 2023;473:145381. DOI
15. Soloveichik G. Electrochemical synthesis of ammonia as a potential alternative to the Haber-Bosch process. *Nat Catal* 2019;2:377-80. DOI
16. El-shafie M, Kambara S. Recent advances in ammonia synthesis technologies: toward future zero carbon emissions. *Int J Hydrog Energy* 2023;48:11237-73. DOI
17. Lazouski N, Chung M, Williams K, Gala ML, Manthiram K. Non-aqueous gas diffusion electrodes for rapid ammonia synthesis from nitrogen and water-splitting-derived hydrogen. *Nat Catal* 2020;3:463-9. DOI
18. Verleysen K, Parente A, Contino F. How sensitive is a dynamic ammonia synthesis process? Global sensitivity analysis of a dynamic Haber-Bosch process (for flexible seasonal energy storage). *Energy* 2021;232:121016. DOI
19. Guo J, Chen P. Catalyst: NH<sub>3</sub> as an energy carrier. *Chem* 2017;3:709-12. DOI
20. Zhang L, Ji X, Ren X, et al. Electrochemical ammonia synthesis via nitrogen reduction reaction on a MoS<sub>2</sub> catalyst: theoretical and experimental studies. *Adv Mater* 2018;30:e1800191. DOI
21. Montoya JH, Tsai C, Vojvodic A, Nørskov JK. The challenge of electrochemical ammonia synthesis: a new perspective on the role of nitrogen scaling relations. *ChemSusChem* 2015;8:2180-6. DOI PubMed
22. Wu D, Peng X, Li L, et al. Commercial biogas plants: review on operational parameters and guide for performance optimization. *Fuel* 2021;303:121282. DOI
23. Giddey S, Badwal S, Kulkarni A. Review of electrochemical ammonia production technologies and materials. *Int J Hydrog Energy* 2013;38:14576-94. DOI
24. Shen H, Choi C, Masa J, et al. Electrochemical ammonia synthesis: mechanistic understanding and catalyst design. *Chem* 2021;7:1708-54. DOI
25. Long J, Chen S, Zhang Y, et al. Direct electrochemical ammonia synthesis from nitric oxide. *Angew Chem Int Ed* 2020;59:9711-8. DOI
26. Jiang H, Chen GF, Hai G, et al. A nitrogen battery electrode involving eight-electron transfer per nitrogen for energy storage. *Angew Chem Int Ed* 2023;62:e202305695. DOI
27. Smith C, Hill AK, Torrente-murciano L. Current and future role of Haber-Bosch ammonia in a carbon-free energy landscape. *Energy Environ Sci* 2020;13:331-44. DOI
28. Thakur IS, Medhi K. Nitrification and denitrification processes for mitigation of nitrous oxide from waste water treatment plants for biovalorization: challenges and opportunities. *Bioresour Technol* 2019;282:502-13. DOI PubMed
29. Hon WM, Lee KH, Khoo HE. Nitric oxide in liver diseases: friend, foe, or just passerby? *Ann N Y Acad Sci* 2002;962:275-95. DOI PubMed
30. Knobeloch L, Salna B, Hogan A, Postle J, Anderson H. Blue babies and nitrate-contaminated well water. *Environ Health Perspect* 2000;108:675-8. DOI PubMed PMC
31. WHO. Nitrate and nitrite in drinking-water. 2016. Available from: <https://www.who.int/docs/default-source/wash-documents/wash-chemicals/nitrate-nitrite-background-document.pdf> [Last accessed on 20 Feb 2024].
32. Schoeman J, Steyn A. Nitrate removal with reverse osmosis in a rural area in South Africa. *Desalination* 2003;155:15-26. DOI
33. Clifford D, Liu X. Ion exchange for nitrate removal. *J Am Water Works Assoc* 1993;85:135-43. DOI
34. Wei L, Liu D, Rosales BA, Evans JW, Vela J. Mild and selective hydrogenation of nitrate to ammonia in the absence of noble metals. *ACS Catal* 2020;10:3618-28. DOI
35. Zhang X, Wang Y, Liu C, Yu Y, Lu S, Zhang B. Recent advances in non-noble metal electrocatalysts for nitrate reduction. *Chem Eng J* 2021;403:126269. DOI
36. Xu H, Ma Y, Chen J, Zhang WX, Yang J. Electrocatalytic reduction of nitrate - a step towards a sustainable nitrogen cycle. *Chem Soc Rev* 2022;51:2710-58. DOI
37. Wang Y, Shu S, Peng M, et al. Dual-site electrocatalytic nitrate reduction to ammonia on oxygen vacancy-enriched and Pd-decorated MnO<sub>2</sub> nanosheets. *Nanoscale* 2021;13:17504-11. DOI
38. Cui Y, Yang H, Dai C, Ren P, Song C, Ma X. Coupling of LaFeO<sub>3</sub> - plasma catalysis and Cu<sup>+</sup>/Cu<sup>0</sup> electrocatalysis for direct ammonia synthesis from air. *Ind Eng Chem Res* 2022;61:4816-23. DOI
39. Deng X, Yang Y, Wang L, Fu XZ, Luo JL. Metallic Co nanoarray catalyzes selective NH<sub>3</sub> production from electrochemical nitrate reduction at current densities exceeding 2 A cm<sup>-2</sup>. *Adv Sci* 2021;8:2004523. DOI PubMed PMC
40. Rosca V, Duca M, de Groot MT, Koper MT. Nitrogen cycle electrocatalysis. *Chem Rev* 2009;109:2209-44. DOI PubMed
41. Jung W, Hwang YJ. Material strategies in the electrochemical nitrate reduction reaction to ammonia production. *Mater Chem Front* 2021;5:6803-23. DOI
42. Wang Q, Zhao X, Zhang J, Zhang X. Investigation of nitrate reduction on polycrystalline Pt nanoparticles with controlled crystal

- plane. *J Electroanal Chem* 2015;755:210-4. DOI
43. Lim J, Liu C, Park J, et al. Structure sensitivity of Pd facets for enhanced electrochemical nitrate reduction to ammonia. *ACS Catal* 2021;11:7568-77. DOI
  44. Liu H, Park J, Chen Y, et al. Electrocatalytic nitrate reduction on oxide-derived silver with tunable selectivity to nitrite and ammonia. *ACS Catal* 2021;11:8431-42. DOI
  45. Siriwatcharapiboon W, Kwon Y, Yang J, et al. Promotion effects of Sn on the electrocatalytic reduction of nitrate at Rh nanoparticles. *ChemElectroChem* 2014;1:172-9. DOI
  46. Wang Y, Zhou W, Jia R, Yu Y, Zhang B. Unveiling the activity origin of a copper-based electrocatalyst for selective nitrate reduction to ammonia. *Angew Chem Int Ed* 2020;59:5350-4. DOI
  47. He W, Zhang J, Dieckhöfer S, et al. Splicing the active phases of copper/cobalt-based catalysts achieves high-rate tandem electroreduction of nitrate to ammonia. *Nat Commun* 2022;13:1129. DOI PubMed PMC
  48. Wang C, Ye F, Shen J, Xue KH, Zhu Y, Li C. In situ loading of Cu<sub>2</sub>O active sites on island-like copper for efficient electrochemical reduction of nitrate to ammonia. *ACS Appl Mater Interfaces* 2022;14:6680-8. DOI
  49. Anastasiadou D, van Beek Y, Hensen EJM, Costa Figueiredo M. Ammonia electrocatalytic synthesis from nitrate. *Electrochem Sci Adv* 2023;3:e2100220. DOI
  50. Chia X, Pumera M. Characteristics and performance of two-dimensional materials for electrocatalysis. *Nat Catal* 2018;1:909-21. DOI
  51. Tao H, Fan Q, Ma T, et al. Two-dimensional materials for energy conversion and storage. *Prog Mater Sci* 2020;111:100637. DOI
  52. Du F, Li J, Wang C, et al. Active sites-rich layered double hydroxide for nitrate-to-ammonia production with high selectivity and stability. *Chem Eng J* 2022;434:134641. DOI
  53. Kim K, Lee H, Huang X, et al. Energy-efficient electrochemical ammonia production from dilute nitrate solution. *Energy Environ Sci* 2023;16:663-72. DOI
  54. Li J, Zhang Y, Liu C, et al. 3.4% Solar-to-ammonia efficiency from nitrate using Fe single atomic catalyst supported on MoS<sub>2</sub> nanosheets. *Adv Funct Mater* 2022;32:2108316. DOI
  55. Li H, Xu X, Lin X, et al. Cooperative interaction between Cu and sulfur vacancies in SnS<sub>2</sub> nanoflowers for highly efficient nitrate electroreduction to ammonia. *J Mater Chem A* 2023;11:2014-22. DOI
  56. Li Y, Ma J, Waite TD, Hoffmann MR, Wang Z. Development of a mechanically flexible 2D-MXene membrane cathode for selective electrochemical reduction of nitrate to N<sub>2</sub>: mechanisms and implications. *Environ Sci Technol* 2021;55:10695-703. DOI
  57. Karthikeyan P, Elanchezhian S, Preethi J, Talukdar K, Meenakshi S, Park CM. Two-dimensional (2D) Ti<sub>3</sub>C<sub>2</sub>T<sub>x</sub> MXene nanosheets with superior adsorption behavior for phosphate and nitrate ions from the aqueous environment. *Ceram Int* 2021;47:732-9. DOI
  58. Pan F, Zhou J, Wang T, et al. Revealing the activity origin of ultrathin nickel metal-organic framework nanosheet catalysts for selective electrochemical nitrate reduction to ammonia: experimental and density functional theory investigations. *J Colloid Interface Sci* 2023;638:26-38. DOI
  59. Sivan SE, Kang KH, Han SJ, et al. Facile MOF-derived one-pot synthetic approach toward Ru single atoms, nanoclusters, and nanoparticles dispersed on CeO<sub>2</sub> supports for enhanced ammonia synthesis. *J Catal* 2022;408:316-28. DOI
  60. Wang H, Guo Y, Li C, et al. Cu/CuO<sub>x</sub> in-plane heterostructured nanosheet arrays with rich oxygen vacancies enhance nitrate electroreduction to ammonia. *ACS Appl Mater Interfaces* 2022;14:34761-9. DOI
  61. Zhao F, Hai G, Li X, Jiang Z, Wang H. Enhanced electrocatalytic nitrate reduction to ammonia on cobalt oxide nanosheets via multiscale defect modulation. *Chem Eng J* 2023;461:141960. DOI
  62. Wu ZY, Karamad M, Yong X, et al. Electrochemical ammonia synthesis via nitrate reduction on Fe single atom catalyst. *Nat Commun* 2021;12:2870. DOI PubMed PMC
  63. Wang H, Liu X, Niu P, Wang S, Shi J, Li L. Porous Two-dimensional materials for photocatalytic and electrocatalytic applications. *Matter* 2020;2:1377-413. DOI
  64. Jia R, Wang Y, Wang C, Ling Y, Yu Y, Zhang B. Boosting selective nitrate electroreduction to ammonium by constructing oxygen vacancies in TiO<sub>2</sub>. *ACS Catal* 2020;10:3533-40. DOI
  65. Liu Y, Deng P, Wu R, Zhang X, Sun C, Li H. Oxygen vacancies for promoting the electrochemical nitrogen reduction reaction. *J Mater Chem A* 2021;9:6694-709. DOI
  66. Wang C, Liu Z, Hu T, et al. Metasequoia-like nanocrystal of iron-doped copper for efficient electrocatalytic nitrate reduction into ammonia in neutral media. *ChemSusChem* 2021;14:1825-9. DOI
  67. Cui X, Tang C, Zhang Q. A review of electrocatalytic reduction of dinitrogen to ammonia under ambient conditions. *Adv Energy Mater* 2018;8:1800369. DOI
  68. Chen G, Ren S, Zhang L, et al. Advances in electrocatalytic N<sub>2</sub> reduction - strategies to tackle the selectivity challenge. *Small Methods* 2019;3:1800337. DOI
  69. Wang Q, O'Hare D. Recent advances in the synthesis and application of layered double hydroxide (LDH) nanosheets. *Chem Rev* 2012;112:4124-55. DOI PubMed
  70. Yi H, Liu S, Lai C, et al. Recent advance of transition-metal-based layered double hydroxide nanosheets: synthesis, properties, modification, and electrocatalytic applications. *Adv Energy Mater* 2021;11:2002863. DOI
  71. Zhang S, Zhao Y, Shi R, et al. Efficient photocatalytic nitrogen fixation over Cu<sup>δ+</sup>-modified defective ZnAl-layered double hydroxide nanosheets. *Adv Energy Mater* 2020;10:1901973. DOI

72. Li T, Li R, Luo H. Facile in situ growth of Ni/Co-LDH arrays by hypothermal chemical coprecipitation for all-solid-state asymmetric supercapacitors. *J Mater Chem A* 2016;4:18922-30. DOI
73. Xu J, Deng H, Song J, Zhao J, Zhang L, Hou W. Synthesis of hierarchical flower-like Mg<sub>2</sub>Al-Cl layered double hydroxide in a surfactant-free reverse microemulsion. *J Colloid Interface Sci* 2017;505:816-23. DOI
74. Li J, Lian R, Wang J, He S, Jiang SP, Rui Z. Oxygen vacancy defects modulated electrocatalytic activity of iron-nickel layered double hydroxide on Ni foam as highly active electrodes for oxygen evolution reaction. *Electrochim Acta* 2020;331:135395. DOI
75. Li L, Yang J, Yun Y, Hu S, Huang Y. Characterization and electrochemical behaviour of nanoscale hydrotalcite-like compounds toward the reduction of nitrate. *Nanomaterials* 2020;10:1926. DOI PubMed PMC
76. Yu MS, Jesudass SC, Surendran S, Kim JY, Sim U, Han MK. Synergistic interaction of MoS<sub>2</sub> nanoflakes on La<sub>2</sub>Zr<sub>2</sub>O<sub>7</sub> nanofibers for improving photoelectrochemical nitrogen reduction. *ACS Appl Mater Interfaces* 2022;14:31889-99. DOI PubMed
77. Whittingham MS. Lithium batteries and cathode materials. *Chem Rev* 2004;104:4271-301. DOI PubMed
78. Choi W, Choudhary N, Han GH, Park J, Akinwande D, Lee YH. Recent development of two-dimensional transition metal dichalcogenides and their applications. *Mater Today* 2017;20:116-30. DOI
79. Sukanya R, da Silva Alves DC, Breslin CB. Review - recent developments in the applications of 2D transition metal dichalcogenides as electrocatalysts in the generation of hydrogen for renewable energy conversion. *J Electrochem Soc* 2022;169:064504. DOI
80. Wang J, Sun Z, Li Y, et al. Sulfur vacancy MoS<sub>2</sub> for electrocatalytic reduction of nitrate to ammonia with enhanced selectivity. *J Alloys Compd* 2023;955:170199. DOI
81. Mohanty B, Jena BK, Basu S. Single atom on the 2D matrix: an emerging electrocatalyst for energy applications. *ACS Omega* 2020;5:1287-95. DOI PubMed PMC
82. Fan M, Cui J, Wu J, Vajtai R, Sun D, Ajayan PM. Improving the catalytic activity of carbon-supported single atom catalysts by polynary metal or heteroatom doping. *Small* 2020;16:e1906782. DOI
83. Ding J, Hou X, Qiu Y, et al. Iron-doping strategy promotes electroreduction of nitrate to ammonia on MoS<sub>2</sub> nanosheets. *Inorg Chem Commun* 2023;151:110621. DOI
84. Xu T, Liang J, Li S, et al. Recent advances in nonprecious metal oxide electrocatalysts and photocatalysts for N<sub>2</sub> reduction reaction under ambient condition. *Small Sci* 2021;1:2000069. DOI
85. Cui X, Tang C, Liu XM, Wang C, Ma W, Zhang Q. Highly selective electrochemical reduction of dinitrogen to ammonia at ambient temperature and pressure over iron oxide catalysts. *Chemistry* 2018;24:18494-501. DOI PubMed
86. Xiong W, Yin H, Wu T, Li H. Challenges and opportunities of transition metal oxides as electrocatalysts. *Chemistry* 2023;29:e202202872. DOI PubMed
87. Sun Z, Liao T, Dou Y, et al. Generalized self-assembly of scalable two-dimensional transition metal oxide nanosheets. *Nat Commun* 2014;5:3813. DOI
88. Sun Y, Liu Q, Gao S, et al. Pits confined in ultrathin cerium(IV) oxide for studying catalytic centers in carbon monoxide oxidation. *Nat Commun* 2013;4:2899. DOI
89. Huang Z, Zhou A, Wu J, et al. Bottom-up preparation of ultrathin 2D aluminum oxide nanosheets by duplicating graphene oxide. *Adv Mater* 2016;28:1703-8. DOI
90. Li C, Liu L, Kang J, et al. Pristine MOF and COF materials for advanced batteries. *Energy Stor Mater* 2020;31:115-34. DOI
91. Sheberla D, Bachman JC, Elias JS, Sun CJ, Shao-Horn Y, Dincă M. Conductive MOF electrodes for stable supercapacitors with high areal capacitance. *Nat Mater* 2017;16:220-4. DOI PubMed
92. Wang Q, Astruc D. State of the art and prospects in metal-organic framework (MOF)-based and MOF-derived nanocatalysis. *Chem Rev* 2020;120:1438-511. DOI PubMed
93. Wu T, Liu X, Liu Y, et al. Application of QD-MOF composites for photocatalysis: energy production and environmental remediation. *Coord Chem Rev* 2020;403:213097. DOI
94. Ma T, Li H, Ma JG, Cheng P. Application of MOF-based materials in electrochemical sensing. *Dalton Trans* 2020;49:17121-9. DOI PubMed
95. Chae HK, Siberio-Pérez DY, Kim J, et al. A route to high surface area, porosity and inclusion of large molecules in crystals. *Nature* 2004;427:523-7. DOI
96. Freund R, Zaremba O, Arnauts G, et al. The current status of MOF and COF applications. *Angew Chem Int Ed* 2021;60:23975-4001. DOI
97. Wang J, Li N, Xu Y, Pang H. Two-dimensional MOF and COF nanosheets: synthesis and applications in electrochemistry. *Chemistry* 2020;26:6402-22. DOI
98. Lv Y, Su J, Gu Y, et al. Atomically precise integration of multiple functional motifs in catalytic metal-organic frameworks for highly efficient nitrate electroreduction. *JACS Au* 2022;2:2765-77. DOI
99. Liu P, Yan J, Huang H, Song W. Cu/Co bimetallic conductive MOFs: electronic modulation for enhanced nitrate reduction to ammonia. *Chem Eng J* 2023;466:143134. DOI
100. Fang Z, Jin Z, Tang S, Li P, Wu P, Yu G. Porous two-dimensional iron-cyano nanosheets for high-rate electrochemical nitrate reduction. *ACS Nano* 2022;16:1072-81. DOI
101. Zhang T, Pan L, Tang H, et al. Synthesis of two-dimensional Ti<sub>3</sub>C<sub>2</sub>T<sub>x</sub> MXene using HCl+LiF etchant: enhanced exfoliation and delamination. *J Alloys Compd* 2017;695:818-26. DOI
102. Ihsanullah I. MXenes (two-dimensional metal carbides) as emerging nanomaterials for water purification: progress, challenges and

- prospects. *Chem Eng J* 2020;388:124340. DOI
103. Wyatt BC, Rosenkranz A, Anasori B. 2D MXenes: tunable mechanical and tribological properties. *Adv Mater* 2021;33:e2007973. DOI PubMed
104. Qian A, Seo JY, Shi H, Lee JY, Chung CH. Surface functional groups and electrochemical behavior in dimethyl sulfoxide-delaminated  $Ti_3C_2T_x$  MXene. *ChemSusChem* 2018;11:3719-23. DOI
105. Tsounis C, Kumar PV, Masood H, et al. Advancing MXene electrocatalysts for energy conversion reactions: surface, stoichiometry, and stability. *Angew Chem Int Ed* 2023;62:e202210828. DOI PubMed PMC
106. Yorulmaz U, Özden A, Perkgöz NK, Ay F, Sevik C. Vibrational and mechanical properties of single layer MXene structures: a first-principles investigation. *Nanotechnology* 2016;27:335702. DOI PubMed
107. Wu Y, Nie P, Wu L, Dou H, Zhang X. 2D MXene/SnS<sub>2</sub> composites as high-performance anodes for sodium ion batteries. *Chem Eng J* 2018;334:932-8. DOI
108. Wu B, Cai X, Shui L, Gao E, Liu Z. Extraordinary electromechanical actuation of Ti<sub>2</sub>C MXene. *J Phys Chem C* 2021;125:1060-8. DOI
109. Hu C, Du Z, Wei Z, Li L, Shen G. Functionalized Ti<sub>3</sub>C<sub>2</sub>T<sub>x</sub> MXene with layer-dependent band gap for flexible NIR photodetectors. *Appl Phys Rev* 2023;10:021402. DOI
110. Er D, Li J, Naguib M, Gogotsi Y, Shenoy VB. Ti<sub>3</sub>C<sub>2</sub> MXene as a high capacity electrode material for metal (Li, Na, K, Ca) ion batteries. *ACS Appl Mater Interfaces* 2014;6:11173-9. DOI
111. Yang Q, Huang Z, Li X, et al. A wholly degradable, rechargeable Zn-Ti<sub>3</sub>C<sub>2</sub> MXene capacitor with superior anti-self-discharge function. *ACS Nano* 2019;13:8275-83. DOI
112. Le TA, Tran NQ, Hong Y, Kim M, Lee H. Porosity-engineering of MXene as a support material for a highly efficient electrocatalyst toward overall water splitting. *ChemSusChem* 2020;13:945-55. DOI
113. Zhou Z, Yu F, You Y, Zhan J, Zhang L. Tunable functional groups on MXene regulating the catalytic property of anchored cobalt phthalocyanine for electrochemical CO<sub>2</sub> reduction. *Inorg Chem Front* 2023;10:5371-8. DOI
114. Wang X, Bak S, Han M, et al. Surface redox pseudocapacitance of partially oxidized titanium carbide mxene in water-in-salt electrolyte. *ACS Energy Lett* 2022;7:30-5. DOI
115. Cai J, Huang J, Cao A, et al. Interfacial hydrogen bonding-involved electrocatalytic ammonia synthesis on OH-terminated MXene. *Appl Catal B* 2023;328:122473. DOI
116. Hu T, Wang M, Guo C, Li CM. Functionalized MXenes for efficient electrocatalytic nitrate reduction to ammonia. *J Mater Chem A* 2022;10:8923-31. DOI
117. Brownson DA, Kampouris DK, Banks CE. An overview of graphene in energy production and storage applications. *J Power Sources* 2011;196:4873-85. DOI
118. Zhuo HY, Zhang X, Liang JX, Yu Q, Xiao H, Li J. Theoretical understandings of graphene-based metal single-atom catalysts: stability and catalytic performance. *Chem Rev* 2020;120:12315-41. DOI
119. Cheng N, Zhang L, Doyle-davis K, Sun X. Single-atom catalysts: from design to application. *Electrochem Energy Rev* 2019;2:539-73. DOI
120. Rehman F, Kwon S, Musgrave CB, Tamtaji M, Goddard WA, Luo Z. High-throughput screening to predict highly active dual-atom catalysts for electrocatalytic reduction of nitrate to ammonia. *Nano Energy* 2022;103:107866. DOI
121. Zhao T, Chen K, Xu X, et al. Homonuclear dual-atom catalysts embedded on N-doped graphene for highly efficient nitrate reduction to ammonia: from theoretical prediction to experimental validation. *Appl Catal B* 2023;339:123156. DOI
122. Huang L, Cheng L, Ma T, et al. Direct synthesis of ammonia from nitrate on amorphous graphene with near 100% efficiency. *Adv Mater* 2023;35:e2211856. DOI
123. Luo Y, Chen K, Shen P, et al. B-doped MoS<sub>2</sub> for nitrate electroreduction to ammonia. *J Colloid Interface Sci* 2023;629:950-7. DOI
124. Li J, Liu H, Du F, et al. Microenvironmental corrosion and hydrolysis induced two-dimensional heterojunction of copper oxide@ferrihydrite for efficient electrochemical nitrate reduction to ammonia. *Chem Eng J* 2023;471:144488. DOI
125. Wang S, Song C, Cai Y, et al. Interfacial polarization triggered by covalent-bonded MXene and black phosphorus for enhanced electrochemical nitrate to ammonia conversion. *Adv Energy Mater* 2023;13:2301136. DOI
126. Zhang H, Li L, Sun W, He J, Xu Q, Lu J. Highly dispersed in-situ grown Bi<sub>2</sub>O<sub>3</sub> nanosheets on Ti<sub>3</sub>C<sub>2</sub>T<sub>x</sub> MXene for selective electroreduction of nitrate to ammonia. *ChemElectroChem* 2023;10:e202201001. DOI
127. Wang Y, Rahimnejad S, Sun WJ, et al. Bimetallic Cu-Fe catalysts on MXene for synergistically electrocatalytic conversion of nitrate to ammonia. *J Colloid Interface Sci* 2023;648:595-603. DOI
128. Sun W, Li L, Zhang H, He J, Lu J. A bioinspired iron-centered electrocatalyst for selective catalytic reduction of nitrate to ammonia. *ACS Sustain Chem Eng* 2022;10:5958-65. DOI
129. Sun WJ, Ji HQ, Li LX, et al. Built-in electric field triggered interfacial accumulation effect for efficient nitrate removal at ultra-low concentration and electroreduction to ammonia. *Angew Chem Int Ed Engl* 2021;60:22933-9. DOI
130. Zhu D, Li G, Yan X, Geng C, Gao L. Electrochemical nitrate reduction to high-value ammonia on two-dimensional molybdenum carbide nanosheets for nitrate-containing wastewater upcycling. *Sci Total Environ* 2023;878:163145. DOI